

# Dissipative Dynamics of Polymer Phononic Materials

Anastasiia O. Krushynska,\* Antonio S. Gliozzi, Alberto Fina, Dmitry Krushinsky, Daniele Battegazzore, Miguel A. Badillo-Ávila, Mónica Acuautla, Stefano Stassi, Camilla Noè, Nicola M. Pugno, and Federico Bosia

Phononic materials are artificial composites with unprecedented abilities to control acoustic waves in solids. Their performance is mainly governed by their architecture, determining frequency ranges in which wave propagation is inhibited. However, the dynamics of phononic materials also depends on the mechanical and material properties of their constituents. In the case of viscoelastic constituents, such as most polymers, it is challenging to correctly predict the actual dynamic behavior of real phononic structures. Existing studies on this topic either lack experimental evidence or are limited to specific materials and architectures in restricted frequency ranges. A general framework is developed and employed to characterize the dynamics of polymer phononic materials with different architectures made of both thermoset and thermoplastic polymers, presenting qualitatively different viscoelastic behaviors. Through a comparison of experimental results with numerical predictions, the reliability of commonly used elastic and viscoelastic material models is evaluated in broad frequency ranges. Correlations between viscous effects and the two main band-gap formation mechanisms in phononic materials are revealed, and experimentally verified guidelines on how to correctly predict their dissipative response are proposed in a computationally efficient way. Overall, this work provides comprehensive guidelines for the extension of phononics modeling to applications involving dissipative viscoelastic materials.

## 1. Introduction

The dynamic behavior of phononic materials is governed mainly by tailored architectures, rather than by material constituents.<sup>[1–3]</sup> A phononic architecture with periodically distributed


heterogeneities, such as cavities or inclusions, can induce elastic wave scattering,<sup>[4]</sup> sound absorption,<sup>[5]</sup> negative refraction,<sup>[6]</sup> cloaking,<sup>[7]</sup> focusing,<sup>[8]</sup> waveguiding,<sup>[9]</sup> one-way,<sup>[10]</sup> or scattering-free propagation,<sup>[11]</sup> and control thermal conductivity.<sup>[12,13]</sup> These and other fascinating effects, unusual for most materials, have revolutionized conventional concepts on wave control and opened previously unforeseen functionalities and applications.<sup>[14–16]</sup>

An attractive feature of a phononic medium is assumed independence of its dynamic behavior from its constituent materials and structural dimensions. This means that a property observed in a millimeter-size structure is likely to be found in meter-, centimeter- or even nanometer-size structures, if the architecture is preserved.<sup>[17–19]</sup> Hence, phononic materials are often developed and tested at the size scales most suitable for experiments, with subsequent rescaling of their characteristics to desired frequencies.<sup>[20–22]</sup> However, this independence assumption is true only if constituent materials have linear

elastic behavior, as, for example, for infinitesimal strains in metals or ceramics.<sup>[10,17,23,24]</sup> In polymers or concrete, material losses can be sufficiently strong to alter or even suppress phononic functionalities.<sup>[22,25–28]</sup> For instance, viscoelastic damping described by time- and strain-dependent mechanical moduli has

Dr. A. O. Krushynska, Dr. M. A. Badillo-Ávila, Dr. M. Acuautla  
Engineering and Technology Institute Groningen (ENTEG)  
Faculty of Science and Engineering  
University of Groningen  
Nijenborgh 4, Groningen 9747AG, The Netherlands  
E-mail: a.o.krushynska@rug.nl

Prof. A. S. Gliozzi, Prof. A. Fina, Dr. D. Battegazzore, Dr. S. Stassi,  
C. Noè, Dr. F. Bosia  
Department of Applied Science and Technology  
Politecnico di Torino  
Corso Duca degli Abruzzi 24, Torino 10129, Italy

 The ORCID identification number(s) for the author(s) of this article can be found under <https://doi.org/10.1002/adfm.202103424>.

© 2021 The Authors. Advanced Functional Materials published by Wiley-VCH GmbH. This is an open access article under the terms of the Creative Commons Attribution NonCommercial License, which permits use, distribution and reproduction in any medium, provided the original work is properly cited and is not used for commercial purposes.

DOI: 10.1002/adfm.202103424

Dr. D. Krushinsky  
Operations Research and Logistics  
Wageningen University & Research  
Hollandseweg 1, Wageningen 6706 KN, The Netherlands

Prof. N. M. Pugno  
Laboratory of Bio-inspired, Bionic, Nano, Meta Materials & Mechanics  
Department of Civil, Environmental and Mechanical Engineering  
University of Trento  
Via Mesiano, 77, Trento 38123, Italy

Prof. N. M. Pugno  
School of Engineering and Materials Science  
Queen Mary University of London  
Mile End Road, London E1 4NS, UK

truly multiscale effects on phononic materials: the damping is governed by the microstructure of a constituent material at the molecular level, by the size and shape of mesoscopic units (e.g., thin structural elements), and by topology and structural sizes at the macrostructural level (e.g., plates or beams). This multi-level dependence complicates the analysis of wave dynamics in dissipative phononic materials and introduces uncertainties about their real performance. As a result, the design and development of reliable phononic technologies are considerably challenging. Hence, there is a need to identify key viscoelastic effects for a variety of constituent materials and correlate them to a limitless design space of phononic materials at various size scales.

To address this challenge, it is necessary to link the vast amount of knowledge available in the field of viscoelasticity to wave control mechanisms occurring in phononic materials, and study the interplay between material and architectural characteristics at different scales from the theoretical and experimental points of view.

Viscoelastic effects on phononic materials have been studied analytically by means of single-parameter models<sup>[22,26,27,29–37]</sup> and numerically by using multi-parameter models.<sup>[9,26,36,38]</sup> These and other unmentioned studies provide useful insights into the influence of viscous losses on wave propagation and report basic effects of damping on wave scattering in phononic media. However, it remains unclear to which extent the derived conclusions are applicable to real phononic materials, due to the lack of experimental data and to simplified modeling where a single parameter is used to capture multi-scale relaxation.<sup>[39–41]</sup>

In this work, we propose a comprehensive and general approach to modeling wave dynamics in dissipative phononic media, capable of addressing the complexity of this problem in full. The remainder of this paper is organized as follows. First, we briefly overview the basic principles of the viscoelasticity theory and classify polymers according to their mechanical and chemical properties. Then, we present measured viscoelastic characteristics of two main classes of polymers and derive master curves to describe their mechanical moduli at the frequencies of interest. Next, we fit the master curves by means of multi-mode Maxwell models using a novel flexible and computationally efficient procedure. The obtained frequency-dependent moduli are then used to characterize wave dispersion and transmission in phononic materials with two wave scattering mechanisms by means of the finite-element analysis. The numerical predictions based on linear elastic or viscoelastic models are compared with experimental data on ad-hoc manufactured specimens with various architectures, in order to validate the models in different frequency ranges. In contrast to previous studies, this framework can be applied to analyze any phononic architecture and any constituent material, and allows drawing general conclusions regarding the viscoelastic effects, including the cases when they can be safely neglected.

## 2. Viscoelasticity of Polymers

Dynamic mechanical properties of viscoelastic polymers depend on temperature  $T$  and strain rate  $\dot{\epsilon}$  relaxation.<sup>[42–44]</sup> At room temperature, many amorphous polymers are in a glassy state with predominantly elastic behavior and low losses. As the temperature increases, a polymer changes its state from glassy

to rubbery passing through a glass transition zone.<sup>[39–41]</sup> In this zone, also known as the  $\alpha$  transition, the material behaves viscoelastically, exhibiting a rapid decrease in the storage modulus and a peak for loss factor  $\tan(\delta)$ . The bounds of the zone are governed by the glass transition temperature  $T_g$  which is defined ambiguously in literature.<sup>[45,46]</sup> Here, we define  $T_g$  as the temperature corresponding to the local maximum of loss factor  $\tan(\delta)$  in the  $\alpha$  transition zone, that is,  $T_{\alpha}$ .

Rapid variations of mechanical moduli in the  $\alpha$  transition zone (**Figure 1a**) are caused by motions of the main polymer chains as a consequence of bond rotations in molecules.<sup>[47]</sup> Besides, the polymer backbone can also undergo local movements, or side chains can rotate. These local motions result in additional peaks for  $\tan(\delta)$  that appear in the glassy state at low temperatures and correspond to secondary  $\beta$ ,  $\gamma$ ,... transitions,<sup>[45]</sup> as schematically illustrated in **Figure 1a**.

Additionally, the mechanical properties of polymers are sensitive to strain rate  $\dot{\epsilon}$  relaxation.<sup>[42–44]</sup> In particular, the bounds of the transition zones can vary depending on the excitation frequency as schematically shown in **Figure 1b**. This occurs because at a given temperature larger strain rates decrease molecular mobility, affecting the re-arrangements of macromolecular chains.<sup>[45]</sup> Hence, the  $\alpha$  transitions shift to higher temperatures with increasing strain rate.

If changes in the polymer structure induced by the temperature are equivalent to those induced dynamically, the viscoelastic behavior can be described by means of a time-temperature superposition (TTS) principle.<sup>[40,41]</sup> Thus, an increase in frequency has the same effect as a decrease in temperature, and vice versa, and a polymer is called rheologically simple. Otherwise, a polymer is called rheologically complex. This happens if the temperature shift at larger strain rates strongly depends on the type of relaxation, with larger effects on secondary relaxations ( $\gamma > \beta > \alpha$ ). At high strain rates, this effect may cause an overlap of different relaxation modes, leading to a complex viscoelastic relaxation over broader temperature ranges.<sup>[48,49]</sup>

Apart from viscoelastic characteristics, polymers can be categorized according to their chemical structure and properties, as thermoplastics, thermosets, and elastomers.<sup>[41,50]</sup> In this work, we rely on the assumption of infinitesimal strains. Elastomers are thus excluded from the consideration because they exhibit large deformations.

Thermoplastics contain long polymer chains bound via relatively weak interactions (inset in **Figure 1c**). The chains can easily slide along each other when heated or excited dynamically. The strength of the secondary bonds (van der Waals interactions or H-bonds) linking molecules governs the mechanical properties of a material. An example of a thermoplastic amorphous polymer is polymethylmethacrylate (PMMA). This is a transparent and easy-to-process polymer with a high chemical resistance and good strength. It is widely used as a shatter-resistant and light-weight alternative to glass. The density of pure PMMA is  $1180 \text{ kg m}^{-3}$ ;  $T_g$  values vary from 85 to 140 °C depending on molecular weight, measuring technique, and relevant conditions (e.g., heating rate or strain rate).<sup>[43,51–53]</sup>

Thermosets, in contrast, are composed of dense networks of cross-linked molecules formed during curing, which results in strong primary bonds (inset in **Figure 1d**). High crosslinking density allows retaining a significant storage modulus even above

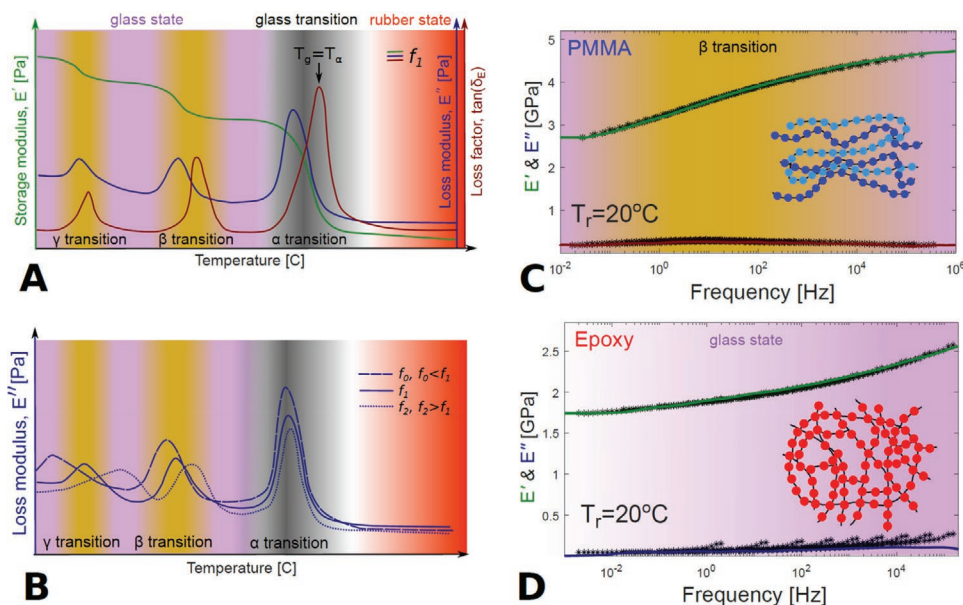


**Figure 1.** Master curves. a) Typical dependence of dynamic mechanical properties of a polymer on temperature at fixed frequency  $f_1$ . b) Typical dependence of the loss modulus of a polymer on temperature at different frequencies. c,d) Experimental (markers) and numerical (solid lines, Arrhenius fit) master curves for the storage and loss moduli of a commercial PMMA and home-made epoxy (DGEBA-TEPA) at reference temperature  $T_r = 20$  °C. The insets schematically represent molecular arrangements in the polymer networks.

$T_g$ . A representative group of thermosets is epoxy resins.<sup>[26,54–57]</sup> They are produced by reacting a multifunctional epoxy compound with a crosslinking agent (commonly, a multifunctional amine), resulting in materials with excellent thermal and chemical resistance, and mechanical properties. The mass density and  $T_g$  of epoxies typically vary between 1100 and 1500 kg m<sup>-3</sup> and 50–180 °C, respectively, depending on the molecular structure, the cross-linking agent, and the cross-linking density.<sup>[44,55,56]</sup>

To understand how the viscoelastic behavior of polymers influences wave attenuation in phononic materials, we focus on PMMA and epoxy resin as representatives of thermoplastics and thermosets, and analyze their material and mechanical characteristics. These materials are often used as constituents of phononic structures.<sup>[4,26,35,58]</sup>

### 3. Material and Mechanical Properties of PMMA and Epoxy

#### 3.1. Material Characterization

Commercial PMMA (ICI Perplex) sheets of 3 and 12 mm thickness acquired from local suppliers were tested as received. To exclude the presence of supplementary components, we performed FTIR analysis that confirmed the composition of a standard PMMA (Section A1.1, Supporting Information). Molecular weight  $M_w^{(p)} = 1474$  kg mol<sup>-1</sup> and molar number  $M_n^{(p)} = 344.7$  kg mol<sup>-1</sup> were estimated by means of gel permeation chromatography (Section A1.2, Supporting Information). Here and further, the superscripts  $p$  and  $e$  refer to the PMMA and the epoxy, respectively. The large molecular weight suggests that the PMMA is casting molded. Hence, it should have a high glass transition temperature ( $T_g > 120$  °C) and a finite storage modulus at temperatures above  $T_g$ .<sup>[43]</sup>

Epoxy plates of the same thicknesses were synthesized from bisphenol-A-diglycidyl ether (DGEBA) and amine tetraethylpentamine (TEPA) (Section A1.3, Supporting Information). To check the material quality, we performed a series of characterization tests. Swelling tests revealed that the epoxy is compact and well-cured with a high crosslinking density of 4 mmol cm<sup>-3</sup> (Section A1.4, Supporting Information). Scanning electron microscopy confirmed a dense composition without major discontinuities, though with randomly distributed small air bubbles that potentially can influence mechanical properties (Section A1.5, Supporting Information). The differential scanning calorimetry (DSC) data disclosed a high  $T_g$  of 134 °C (Section A1.6, Supporting Information). Note that since the DSC detects changes in heat capacity as a function of temperature, these variations cannot be straightforwardly linked to mechanical relaxation in the glass transition governed by an excitation frequency.<sup>[46]</sup> Thus, to evaluate dynamic mechanical properties, we performed dynamic mechanical analysis in temperature (DMTA).

#### 3.2. Viscoelastic Properties

DMTA tests on a single clamped cantilever provide  $T_g^{(p)} = 136$  °C and  $T_g^{(e)} = 148$  °C for the PMMA and the epoxy, respectively, when performing a temperature sweep (2 °C min<sup>-1</sup>) at a constant frequency of 1 Hz (Section A1.7, Supporting Information). These values agree very well with those reported previously.<sup>[43,59]</sup> Besides, both polymers have secondary transition zones.

The  $\beta$  transition for the PMMA occurs at  $\approx 10$  °C, that is, at a local maximum of  $\tan(\delta)$  (Figure A7, Supporting Information) that agrees well with the reported data.<sup>[43,52]</sup> The  $\gamma$  and  $\delta$  secondary transitions are reported below  $-180$  °C,<sup>[43]</sup> thus far

enough in temperature from  $\beta$  to avoid a significant overlap even at relatively high frequencies. Hence, one can expect rheologically simple behavior for the  $\beta$  relaxation of PMMA allowing the application of the TTS principle, as previously suggested, for example, in ref. [60]. The validity of this reasoning is confirmed by a good overlay of the data measured by sweeping frequency at gradually increasing temperatures, thus forming master curves, by applying the TTS principle. These curves are shown in Figure 1c for storage  $E'$  and loss  $E''$  moduli at reference temperature  $T_r = 20$  °C. Tan  $\delta_E$  overlay, shifting factors and Arrhenius fit are reported in Figure A9, Supporting Information, yielding an activation energy of  $\approx 100$  kJ mol<sup>-1</sup>. The derived master curves and activation energy are close to those reported elsewhere<sup>[51–53]</sup> at similar reference temperatures, considering the differences between experimental techniques (single clamped cantilever vs. resonance methods or oscillatory tensile tests) and various grades of PMMA (casting molded vs. extrusion molded). This agreement validates the reliability of our DMTA measurements.

The synthesized epoxy resin presents a broad  $\beta$  transition centered around  $-40$  °C and a weak intermediate relaxation, referred to as  $\omega$ ,<sup>[59]</sup> around  $70$  °C (Figure A8, Supporting Information). In fact, the DMTA plot for our epoxy resin is in a very good agreement with the reported temperatures for the same DGEBA-TEPA epoxy formulation.<sup>[59]</sup> As the molecular structure of crosslinked epoxy resin is intrinsically less regular than that of a simple linear homopolymer such as PMMA, the assignment of a relaxation signal to a precisely defined chain relaxation is quite challenging. González-García et al.<sup>[59]</sup> proposed the  $\beta$  transition for this type of epoxy resin to correspond to a combination of different contributions, including relaxations of hydroxyl ether and diphenyl propane groups, as well as of segments between crosslinking points. The combination of several relaxation modes, possibly having different temperature vs. strain rate dependency, is expected to deliver a complex rheological behavior to this epoxy. Indeed, the DMTA plots obtained by frequency sweeps over varying temperatures provide curves with different slopes that do not satisfactorily overlap into master curves (Figure A10a, Supporting Information). Attempting the Arrhenius fit on the obtained shift factors yields an activation energy of  $\approx 169$  kJ mol<sup>-1</sup>, which appears too high for the  $\beta$  relaxation and is anyway very different from the reported values.<sup>[59]</sup> Hence, we conclude that our epoxy actually behaves as a rheologically complex material. In addition to the overlap of the transition zones, other reasons for this behavior can be dissimilar crosslinking density, irregular arrangement of epoxy groups and/or unreacted segments,<sup>[61]</sup> and dangling chains formed by possibly nonuniform heat dissipation during manufacturing. Hence, reliable extrapolation of viscoelastic behavior at high frequencies does not seem possible based on the available data. Reliable master curves for the epoxy can be obtained under isothermal conditions at broadband frequencies, for example, by viscoelastic spectroscopy<sup>[53]</sup> or resonance techniques.<sup>[52]</sup>

Unfortunately, the measurements of isothermal viscoelastic properties are scarce, especially at room temperature, as most of them are done around  $T_g$ .<sup>[44,45,56,57,61]</sup> Furthermore, a large variety of epoxy compounds makes the extrapolation of appropriate data for our specific epoxy composition impossible. As

broadband isothermal tests require specialized setups unavailable to us (which can also be the case for researchers working on polymer phononic materials), we propose an alternative way to approximate master curves for the rheologically complex epoxy.

We assume that the master curve of the storage modulus obtained by the Arrhenius fit with the shift on  $E'$  can be taken as an acceptable approximation (Figure 1d and Figure A10a, Supporting Information). This can be partially justified by the weak dependency of  $E'$  on temperature, thus minimizing error in extrapolation at high frequencies. For the loss factor, we use a lower envelope curve for the data shifted in the same way (Figure 1d). This approximation captures only the minimum level of the losses and thus does not reproduce them correctly. The only purpose of this is to estimate errors introduced by the approximate material losses on numerical predictions of wave attenuation in phononic materials made of rheologically complex polymers. We emphasize that this approach is applicable only when viscous losses are small, that is,  $\max(\tan\delta_E) < 0.02$ , corresponding to the mechanical properties dominated by the elastic modulus, and cannot deliver meaningful results for larger losses.

For small-amplitude excitations at room temperature, viscous losses in the considered polymers are governed by shear deformation, while volumetric viscosity can be neglected.<sup>[38,52,56]</sup> This occurs because the dispersion of the bulk modulus for the PMMA and epoxy is at least an order of magnitude smaller than that of the shear modulus.<sup>[38,40,52]</sup> The viscoelastic mechanical response of solid polymers below  $T_g$  is typically described by master curves for frequency-dependent Young's modulus  $E$ .<sup>[40,41]</sup> The second mechanical parameter, for example, Poisson's ratio, is often assumed to be fixed. Here, we assign  $\nu^{(p)} = 0.36$ <sup>[52]</sup> and  $\nu^{(e)} = 0.35$ .<sup>[54,59]</sup>

### 3.3. Fitting Experimental Master Curves

Viscoelastic material behavior is often represented by mechanical spring-dashpot models (Section A2.1, Supporting Information). Here, we apply the models commonly used in the studies on viscoelastic phononic materials<sup>[25–27,30–33,35,36,62]</sup> to approximate the master curves of PMMA (Figure 1c) around the  $\beta$  transition zone. The goal is to estimate the accuracy of these models.

One of the simplest models is the standard linear solid model (or Zener model) represented by a spring and a spring-dashpot in series. The Zener model has the following relaxation moduli:<sup>[27,33,62]</sup>

$$E'(\omega) = E_r + \frac{E_1 \omega^2 \tau_1^2}{1 + \omega^2 \tau_1^2}, \quad E''(\omega) = \frac{E_1 \omega \tau_1}{1 + \omega^2 \tau_1^2} \quad (1)$$

where  $\omega = 2\pi f$  is the angular frequency;  $\tau_1 = 1/(2\pi f_{\max})$  defines the most probable relaxation time with  $f_{\max}$  indicating the frequency at maximum losses (Figure 2a). To estimate  $E_1$ , one can fit the storage modulus at  $f_{\max}$ , which gives  $E_1 = 3.67$  GPa (thin curves in Figure 2a). This approximation does not match the experimental data for  $E'$ , and the values of  $E''$  around  $f_{\max}$  are

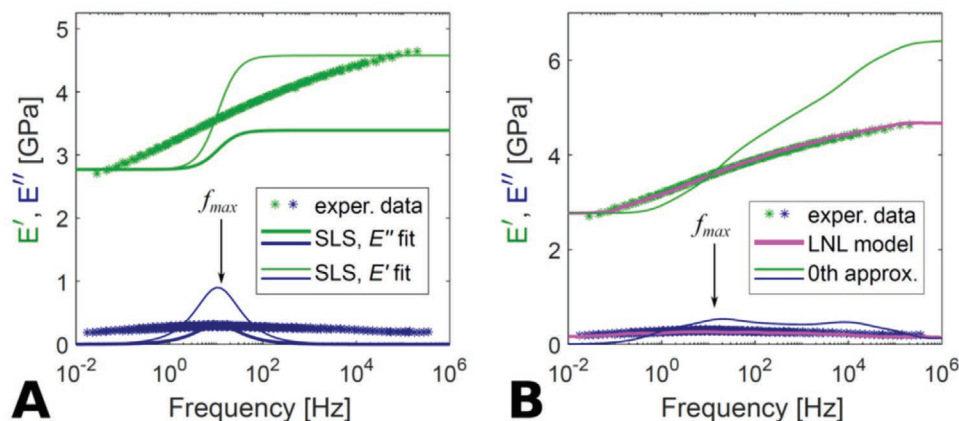


**Figure 2.** Numerical fits (curves) of experimental PMMA master curves (markers) at  $T_r = 20$  °C. a) The SLS model by fitting  $E'$  (thin curves) and  $E''$  (thick curves). b) Fits based on the LNL (thick curves) and zeroth-approximation (thin curves) models.

overestimated. Alternatively,  $E''$  can be matched at  $f_{max}$ , leading to  $E_1 = 0.31$  GPa (thick curves in Figure 2a) that underestimates the measured values at all frequencies. Similar results can be obtained for other values of  $\tau_1$ .

The reason for the inaccuracy of the Zener model is its simplicity due to a single viscous parameter restricting the relaxation zone to limited frequencies. Hence, this model is inaccurate for polymers with transition zones at broad frequencies. The one-parameter Maxwell (a spring and a dashpot in series) and Kelvin–Voigt (a spring and a dashpot in parallel) models suffer from the same drawback.

For polymers with a broadband moduli relaxation, the theory suggests so-called zeroth-order approximation:<sup>[52]</sup>

$$E_n = \frac{4.606E''}{\pi} \text{ at } \tau_n = \frac{1}{2\pi f_n} \quad (2)$$

with  $f_n$  indicating characteristic frequencies, at which strong variations of the moduli occur. The corresponding master curves (thin curves in Figure 2b) show that this model partially captures the frequencies of the PMMA  $\beta$  transition, but overestimates the storage modulus at  $f > f_{max}$ .

A better match can be obtained by using multi-mode models, for example, generalized Maxwell model:

$$E' = E_r + \sum_{n=1}^N \frac{E_n \omega^2 \tau_n^2}{1 + \omega^2 \tau_n^2}, \quad E'' = \sum_{n=1}^N \frac{E_n \omega \tau_n}{1 + \omega^2 \tau_n^2} \quad (3)$$

that has a sufficient number of viscous parameters to capture a full relaxation spectrum. The application of this model requires the estimation of relaxation times  $\tau_n$  and relaxation moduli  $E_r$  and  $E_n$ ,  $n = 1, \dots, N$ . This can be done, for example, by using a least-squares fit of  $E_n$  for prescribed values of  $\tau_n$  in combination with the Tikhonov regularization.<sup>[63]</sup> Obviously, the accuracy of the fit crucially depends on the choice of  $N$  and  $\tau_n$ , which is theoretically unlimited.

As an alternative, we propose a fitting technique with no requirement on the initial choice of  $\tau_n$ . Specifically, both sets of  $E_n$  and  $\tau_n$  are considered unknown, providing more freedom and, potentially, a better fit. We call this technique

a Linear-NonLinear (LNL) model, as the fitting problem is decomposed into a linear and a nonlinear part. In the most general setting, denoting  $C$  as the set of fitting curves, the problem of finding coefficients  $E = (E_n)_{n \in C}$  and  $\tau = (\tau_n)_{n \in C}$  corresponds to solving the following optimization problem:

$$\min_{E, \tau} \left\{ \|F_1(E, \tau) - \gamma_1\|_2 + \alpha \|F_2(E, \tau) - \gamma_2\|_2 \right\} \quad (4)$$

where the notation  $\|\cdot\|_2$  denotes the standard  $l_2$  (Euclidean) norm of a vector. We introduce two vector-valued functions:

$$F_1(E, \tau) = \left( \sum_{i \in C} E_i f_1(\tau_i, x_j) \right)_{j \in P}, \quad F_2(E, \tau) = \left( E_0 + \sum_{i \in C} E_i f_2(\tau_i, x_j) \right)_{j \in P} \quad (5)$$

with  $f_k(x) = \frac{x^k}{1+x^2}$ ,  $k = 1, 2$ . Set  $P$  enumerates the experimental points on the master curves, vector  $x \in \mathbb{R}^{|P|}$  contains the  $\omega$ -values from Equation (3), vectors  $\gamma_1$  and  $\gamma_2$  contain the  $E'$  and  $E''$  values. Parameter  $\alpha$  compensates for the imbalance between the magnitude of values in  $\gamma_1$  and  $\gamma_2$ .

Problem (4)–(5) can be tackled by a variety of techniques, from classic gradient to Nelder–Mead methods.<sup>[64]</sup> However, without additional restrictions, the obtained coefficients are likely to be physically insensible (e.g., negative coefficient values). By adding restrictions directly to problem (4), one obtains a constrained non-linear optimization problem, which is challenging to solve. In contrast, we propose to decompose the problem into a complex but linear part (to optimize  $E$ ) and a smaller non-linear part (to optimize  $\tau$ ). The implementation details are given in Section A2.3, Supporting Information.

The proposed decomposition is crucial for the performance and makes the proposed approach both easy to implement and efficient. Another advantage is its flexibility: due to the fact that the problem of finding the coefficients is under-defined (there exist many sets of coefficients that fit the control points but give unacceptable behavior elsewhere), additional restrictions are necessary. In our approach, adding them is straightforward.

The coefficients  $E_n$  for Equation (3) evaluated by means of the LNL technique (Section A2.3.4, Supporting Information) describe the master curves (thick curves in Figure 2b) that agree very well with the experimental data, proving the high accuracy of the technique.

Equilibrium storage modulus  $E_r$  was estimated by fixing the value of  $E'$  at the lowest frequency, that is,  $E_r^{(p)} = 2.77$  GPa and  $E_r^{(e)} = 1.77$  GPa. These values perfectly agree with those derived from glassy modulus  $E_g = E_r + \sum_{n=1}^N E_n$  that was measured independently by using an ultrasound time-of-flight (ToF) technique. The measured values are  $E_g^{(p)} = 4.91$  GPa,  $E_g^{(e)} = 2.86$  GPa (see Section A2.2, Supporting Information for details).

## 4. Experimental and Numerical Analysis of Viscoelastic Phononic Plates

We consider phononic architectures with periodic patterns in square arrangements, as schematically shown in Figure 3a. The patterns are formed by traversing cruciform cavities or spiral cuts in polymer sheets (Figure 3b). This is a common approach to design phononic plates.<sup>[1,2,65]</sup> Similar configurations have been extensively studied previously and revealed good potential in various applications.<sup>[4,10,17,26,28,58,66,67]</sup>

Each phononic plate is made of both epoxy and PMMA sheets in identical structural dimensions. The cruciform cuts (Figure 3b,c) form patterns with center-to-center distance  $a$  of either 28 mm (Large-cross) or 6 mm (Small-cross) with the aim to activate band gaps at different frequencies (Figures 4a and 5a). The center-to-center distance of the spiral cuts is 25 mm (Spiral, Figure 3b,c) to enable low-frequency band gaps (Figures 4a and 5a). Other geometric parameters of the plates and the manufacturing details can be found in Section A3.1, Supporting Information.

Wave propagation in the plates is analyzed experimentally by measuring transmitted signals (Figure 3d and Section A3.2, Supporting Information) and numerically by means of frequency-domain finite-element simulations (Section A3.3, Supporting Information). Below we present and discuss the obtained results.

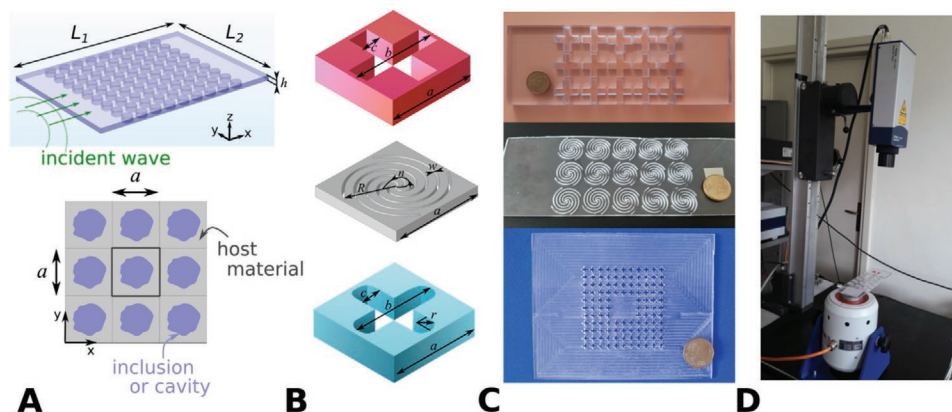


**Figure 3.** Phononic plates geometry and specimens. a) (top) Schematic representation of a phononic plate excited dynamically; (bottom) Top view of the plate with periodic inhomogeneities arranged in a square lattice. b) Unit cells with cruciform and spiral cavities. c) Polymer specimens with cruciform and spiral cavities. d) Experimental setup with a vibration amplifier and laser Doppler vibrometer for transmission measurements.

### 4.1. Transmission Characteristics

We first consider the PMMA plates due to the rheologically simple material behavior. Figure 4b–d shows the dB-level of experimentally measured signals (red curves) transmitted through the Small-cross, Large-cross, and Spiral architectures. The transmission drops of at least 20 dB are classified as experimental band gaps, the bounds of which are indicated by vertical red dashed lines.

The experimental results are used here as a reference to estimate the accuracy of numerical predictions based on different material models. We considered the linear elastic (dashed blue), the viscoelastic Kelvin–Voight (KV, dashed cyan), and the viscoelastic generalized Maxwell (LNL-fit, solid black) models. The linear elastic behavior is specified by the Young's modulus within the experimental band gaps. These values were estimated directly from the master curve for  $E'$  ( $E_{el}$  in Figure 4a). Alternatively, if the master curves are unknown,  $E_{el}$  can be measured by a ToF experiment with a pulse at a central frequency within the band-gap frequencies (Section A2.2, Supporting Information). The same  $E_{el}$  were used in the KV models supplemented by the viscosity parameter  $\eta$ . The value of  $\eta$  can be estimated empirically either by matching numerical to measured transmission curves<sup>[27]</sup> or by keeping viscous losses small at target frequencies.<sup>[26,30,32]</sup> We employed the second approach as it enables to evaluate the accuracy of the KV model. Hence, we assumed  $\eta$  to be equal to 50 Pa·s (Small-cross),  $5 \cdot 10^2$  Pa·s (Large-cross), and  $5 \cdot 10^4$  Pa·s (Spiral). The coefficients of the generalized Maxwell model were obtained by fitting the experimental master curves by the LNL technique (Section A2.3, Supporting Information).

The overall agreement of the numerical results based on the simple models (the linear elastic and viscoelastic KV models) with the experimental data is poor. In contrast, the generalized Maxwell model allows matching the measurements well. Particularly, the simulations based on the simple models roughly predict the band gaps for the Small- and Large-crosses, though they completely fail to estimate the band-gap frequencies for the Spiral plate. This can be due to different band-gap generation mechanisms in the plates. The cruciform cavities activate Bragg scattering that leads to destructive

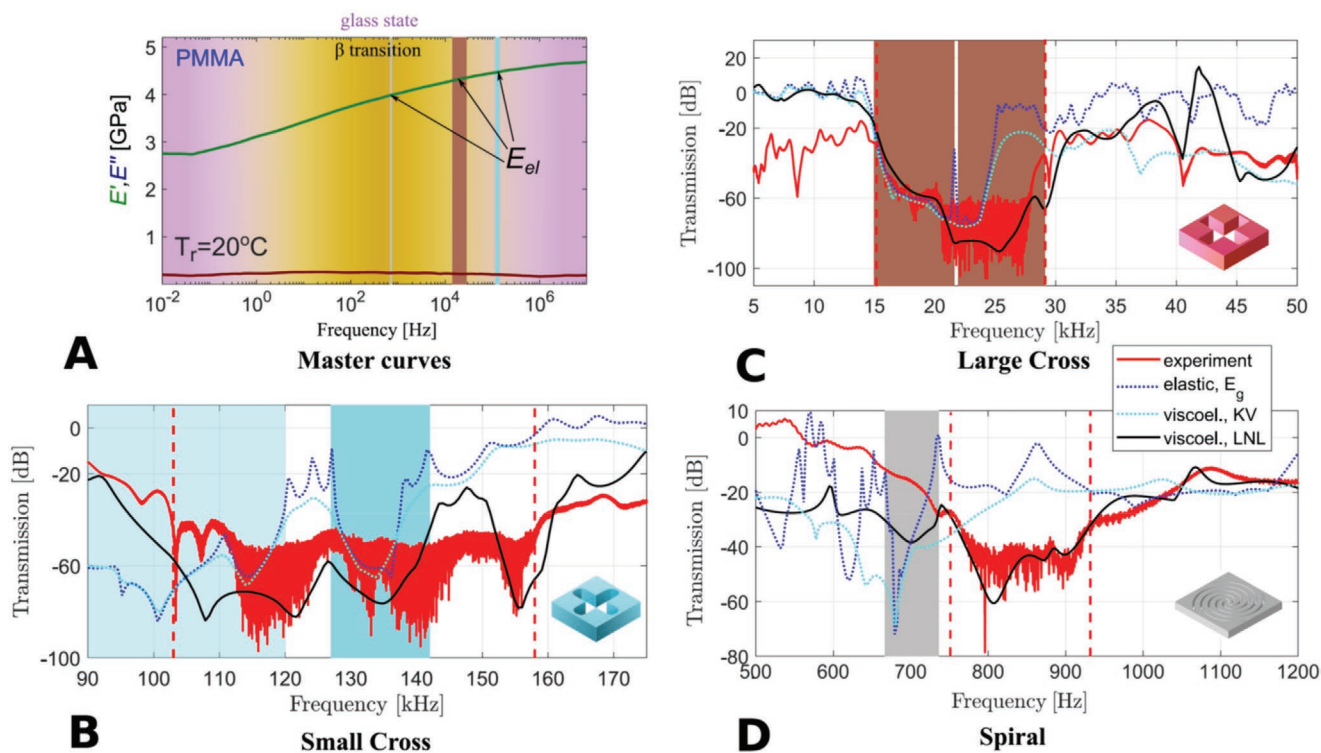


**Figure 4.** Transmission data for the PMMA phononic plates. a) The master curves for the storage and loss moduli reproducing the experimental DMTA data for the PMMA. b–d) The experimental data (red) in comparison with the simulation results for the elastic (dashed blue), viscoelastic generalized Maxwell (LNL, black), and KV (dashed cyan) models. The viscoelastic parameters are given in the text. Vertical red dashed lines indicate the bounds of experimental band gaps; shaded and half-shaded regions correspond to the complete and directional band gaps predicted by the dispersion analysis based on the elastic model.

interference of scattered and incident waves when a half-wavelength is comparable with the lattice period.<sup>[68]</sup> According to previous studies,<sup>[26,30,32]</sup> a Bragg band gap can be extended to broader frequencies due to viscous losses, while its central frequency should be unchanged. This statement was derived for numerical results based on one-parameter viscoelastic models. Our results reveal that the viscoelastic effects can be richer. For instance, the directional and complete band gaps of the Small-cross sample are merged and shifted to higher frequencies due to the losses (Figure 4b).

In the Spiral plate, the curved elements act as resonators when the frequency of incident waves is close to the resonators' eigenfrequency.<sup>[65]</sup> Intense vibrations induced by the resonators can couple to the wave field and inhibit wave propagation, thus generating local-resonance band gaps.<sup>[58,65,69]</sup> The interplay between local resonances and material viscosity substantially influences wave transmission and shifts the band gap to higher frequencies as compared to those predicted by the simple models. Further analysis of the viscoelastic effects on local resonances is given in Section 4.2.

The generalized Maxwell model correctly predicts the band-gap bounds and the trends of the transmission curves around and within the band gaps for both wave attenuation mechanisms and different levels of viscous losses (Figure 4a). The largest discrepancies are observed in the transmission level inside the band gap of the Small-cross plate. This can be due to the manufacturing defects resulting in non-smooth edges

of the crosses that cause additional losses (Figure 3c). The discrepancies at frequencies outside the band gaps can be due to various reasons, for example, differences in the experimental excitation/acquisition and support conditions, imperfect contact between the plate and transducers, transducers sensitivity, etc. The in-depth analysis of these reasons is beyond the scope of this work, which is focused on wave attenuation within band gaps.

We found out that accurate estimations of the band gaps for the PMMA phononic plates require the use of a multi-mode viscoelastic model properly fitting the experimental relaxation moduli (Figure 2b). If the master curves are unavailable, one-parameter viscoelastic or elastic models can suggest approximate band-gap frequencies for plates with Bragg band gaps. However, in these cases, the dispersion analysis can provide comparable approximations (shaded regions in Figure 4b–d) at a lower computational effort (Section 4.2). The accuracy of the dispersion predictions can be even better as the transmission simulations with periodic conditions at lateral faces can include spurious modes localized near the edges. These modes originate from wave reflections at the artificial boundaries and are not damped in the absence of losses, thus reducing the band-gap size (see large transmission values at frequencies close to the upper bound of the second band gap for the small-cross and large-cross plates, Figure 4b–c). Note that in case of local resonances, the simple models completely fail in predicting the band gap (Figure 4d).

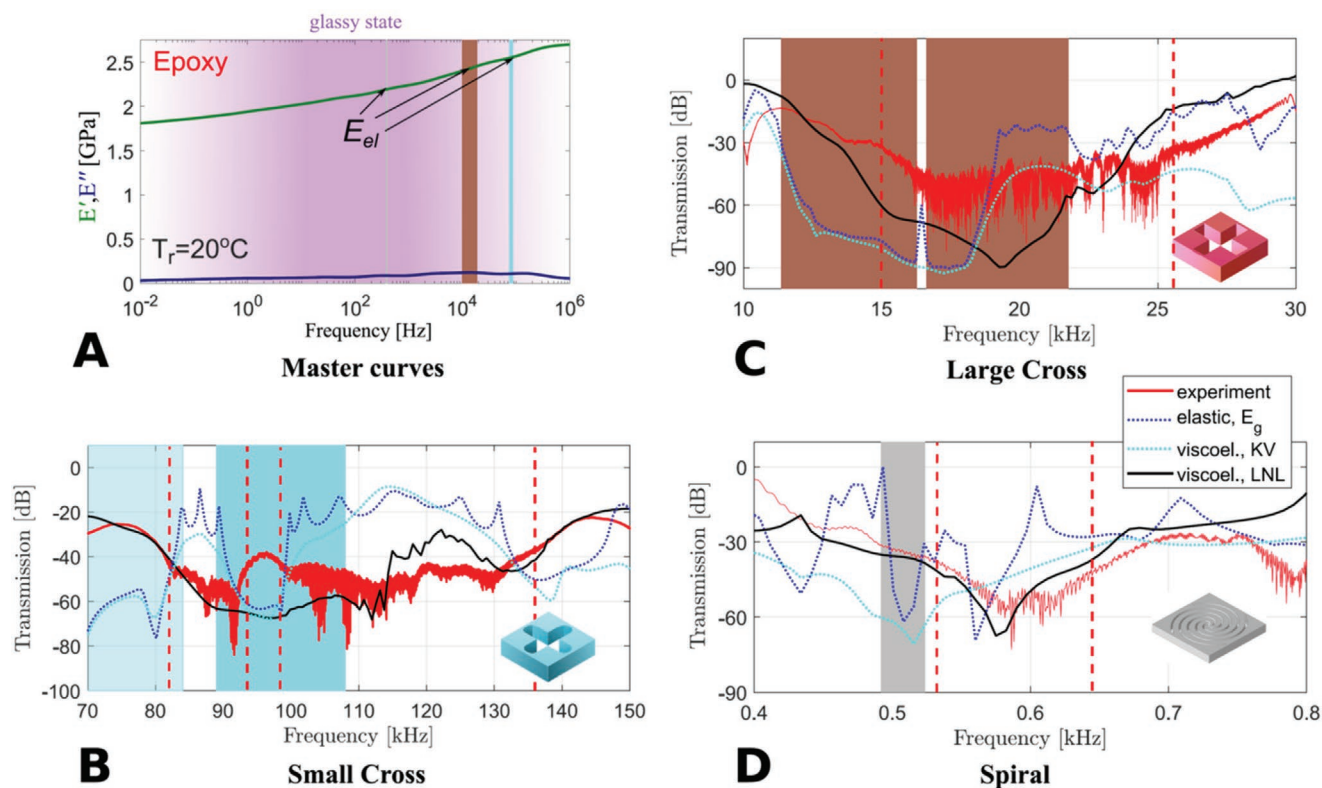


**Figure 5.** Transmission data for the epoxy phononic plates. a) The master curves for the storage and loss moduli approximating the experimental DMTA data for the epoxy. b–d) The experimental data (red) in comparison with the simulation results for the elastic (dashed blue), viscoelastic generalized Maxwell (LNL, black), and KV (dashed cyan) models. The viscoelastic parameters are given in the text. Red dashed lines indicate the bounds of experimental band gaps; shaded and half-shaded regions correspond to the complete and directional band gaps predicted by the dispersion analysis for the elastic model.

Next, we analyze the same phononic samples made of the thermoset epoxy sheets. In the same way as for the PMMA plates, Figure 5b–d shows experimentally measured transmission (red) and the bounds of experimental band gaps marked by vertical red dashed lines. The comparison of the experimental curves in Figures 4 and 5 reveals similarities in the overall trends together with distinctions. The latter include smoother band-gap bounds and less wavy profiles of the curves for the epoxy plates. As the plate architecture is identical, these differences can be attributed only to the rheologically complex behavior of epoxy. We thus have the experimental proof that viscoelastic behavior alters the wave dynamics in phononic plates.

Figure 5b–d also shows numerical transmission curves. The notations and the parameters of the simple models are the same as those for the PMMA plates. This again results in similarities between the curves based on the simple models for the epoxy and the PMMA plates (cf. the dashed blue and cyan curves in Figures 4b–d and 5b–d) provided the distinctions due to different frequency ranges are considered (e.g., cf. Figure A16a,c, Supporting Information). However, in contrast to the PMMA plates, the simple models for the epoxy plates fail to predict the band-gap bounds and the transmission curves for all cases due to the complex material relaxation that cannot be captured by a single viscosity parameter.

Regarding the generalized Maxwell model, we recall that the LNL fit to the experimental master curves (Figure 1d) is

approximate and cannot correctly reproduce viscous losses due to the inapplicability of the TTS principle (Section A1.7, Supporting Information). Hence, it is unreasonable to expect a good match between the numerical (black) and experimental (red) transmission for the epoxy plates. Figure 5b–d shows that it is indeed the case. The comparison of the curves illustrates that the numerical model underestimates real viscous losses, as the calculated band gaps are narrower than the experimental ones. Nevertheless, the multi-mode model approximately predicts both Bragg and locally resonant band gaps, making it still useful for comparison with experimental data and practical applications of phononic plates made of rheologically complex polymers.

#### 4.2. Dispersion Analysis

Wave dispersion in phononic structures is governed by the architecture introducing boundaries or interfaces scattering waves (geometric dispersion) and by material characteristics of constituents (material dispersion). In the case of lossless media, the geometric dispersion can be uncoupled from the material properties by using non-dimensional frequency  $f^* = fa/c$  and wavenumber  $k^* = ka/2\pi$ . Here,  $f$  and  $k$  are the frequency and the wavenumber,  $a$  is the characteristic size, and  $c$  is a fundamental velocity in the medium.<sup>[70]</sup> We assume that



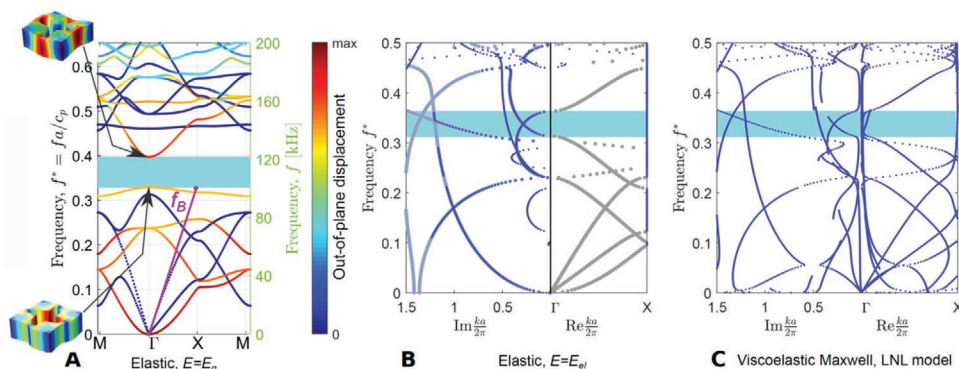


**Figure 6.** Wave dispersion in the Small-cross plate around a Bragg band gap. a) Dispersion diagram for propagating waves with mode shapes at the band-gap bounds ( $E = E_g$ ). The color of the curves indicates the mode polarization ranging from in-plane (blue) to out-of-plane (red). The color in the mode shapes indicates minimum (blue) and maximum (red) displacements. b,c) Dispersion diagrams for propagating and evanescent waves in the  $\Gamma X$  direction for the epoxy plate with elastic  $E = E_{el}$  ( $E_{el} < E_g$ ) and viscoelastic (generalized Maxwell, LNL fit) behavior. Propagating modes are shown by light gray, evanescent modes with complex and imaginary wavenumbers are in light-blue and blue, respectively. The complete band gaps are shaded in blue.

$a$  is the unit cell size and  $c = c_p$ , that is, the ultrasound wave velocity in a polymer plate (Section A2.2, Supporting Information). Then, non-dimensional dispersion diagrams ( $f^*$  vs.  $k^*$ ) for elastic plates of the same architecture, but made of different materials, become identical (Figure A16, Supporting Information) that simplifies the analysis. In the following, we employ non-dimensional terms, if not indicated otherwise.

#### 4.2.1. Bragg Scattering

**Figure 6a** shows the dispersion diagram for waves propagating in the Small-cross medium in terms of non-dimensional and dimensional frequencies for  $E = E_g$ . The band gap shaded in blue originates from the Bragg scattering of longitudinal in-plane waves, since Bragg's frequency  $f_B$  of the fundamental longitudinal mode is close to the band-gap range.<sup>[17,25]</sup> The absence of flat dispersion bands with close to zero group velocity confirms a non-resonant origin of wave scattering at the boundaries of the periodic cavities (see the insets in Figure 6a). Note that in-plane polarized modes (with  $u_z = 0$ , dark blue) exist in the whole analyzed frequency range, while out-of-plane modes (with  $u_x = u_y = 0$ , red) are transformed into mixed modes (with three non-zero displacement components) as frequency increases.

A deeper understanding of the bandgap origin can be obtained by analyzing complete dispersion diagrams, including evanescent modes. Such a diagram is shown in Figure 6b for the  $\Gamma X$  propagation direction in the elastic Small-cross medium with  $E = E_{el}$ . Propagating modes with real-valued wavenumbers are indicated in light gray, the evanescent modes with imaginary and complex-valued wavenumbers are shown in light blue and blue, respectively. Note that the light-gray curves in Figure 6b have similar trends to the curves in the  $\Gamma X$  region of Figure 6a proving weak dependence of the wave dispersion on the material properties in the absence of losses (Section A3.3.2, Supporting Information). Within the band gap, the imaginary branches of the dispersion bands, indicating the level of wave attenuation,<sup>[26]</sup> vary smoothly with a parabola-shaped profile having a maximum at the mid-frequency. This behavior is typical for Bragg's band gaps.<sup>[67]</sup>

If the in-plane dimensions of the Small-cross unit cell are increased by 4.67 times, one obtains the Large-cross unit cell with the dispersion diagram of a similar structure (Figures A13 and A14, Supporting Information). Small variations in the bands' arrangement are attributed to non-proportional scale of the thickness (4.3 times, see also Figure A17, Supporting Information) and to non-rounded corners of the Large-cross cell reducing the ligament stiffness (Figure A18, Supporting Information). The latter leads, for example, to the decrease of the frequency of the third in-plane mode characterized by strong vibrations in the thin ligaments (cf. Figures A16 and A18, Supporting Information). Isotropic scaling of the unit cell dimensions allows to completely preserve the structure of a dispersion diagram (cf. Figure A18b,d, Supporting Information) for the Large-cross plate and for a 10-times Larger plate of the same architecture).

If the constituent medium is viscoelastic, propagating waves are attenuated. The notion of a band gap is then, strictly speaking, elusive, but we still use it to refer to the frequencies corresponding to the elastic band gaps. The losses couple geometric and material dispersion, making a band structure diagram unique for each combination of a phononic pattern and a constituent material. Nevertheless, we continue normalizing the diagrams for the sake of comparison with corresponding elastic cases.

Figure 6c shows a dispersion diagram for the epoxy small-cross unit cell, the viscoelastic behavior of which is described by the generalized Maxwell model. The overall trends of the modes with real wavenumbers are similar to those in the elastic case (Figure 7b), since the material losses are relatively small (Figure 5a). Comparing the diagrams in Figure 6b,c, we can identify two main effects of the viscoelastic material behavior.

The first effect refers to more involute trends of the bands close to the X-point axis in comparison with the elastic case. This occurs due to the coupling between propagating and evanescent modes induced by losses, which also results in "rounding" of the bandgap bounds.<sup>[30]</sup> The second effect is a seemingly larger number of the dispersion bands in the viscoelastic case (cf. Figure 6b,c). The "additional" bands

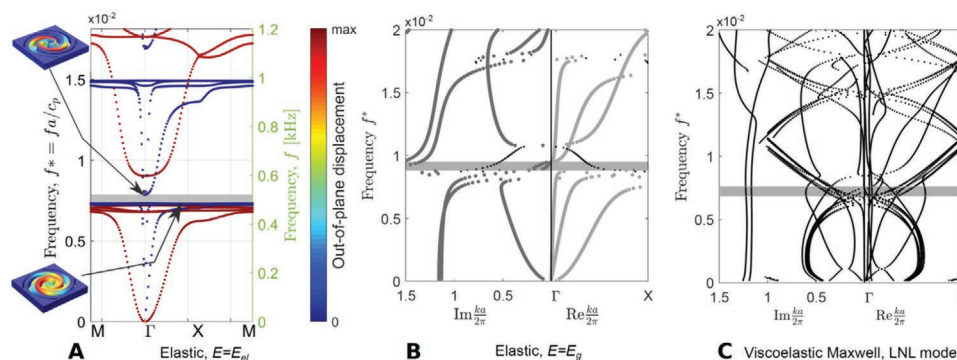


**Figure 7.** Wave dispersion in the Spiral plate around a locally resonant band gap. a) Dispersion diagram for propagating waves with mode shapes at the band-gap bounds. The color of the curves indicates the mode polarization ranging from in-plane (blue) to out-of-plane (red). The color in the mode shapes shows minimum (blue) and maximum (red) displacements. b,c) Dispersion diagrams for propagating and evanescent waves in the  $\Gamma X$  direction for an epoxy plate with elastic or viscoelastic (generalized Maxwell, LNL fit) behavior. Propagating modes are shown by light gray, the evanescent modes with complex and imaginary wavenumbers are indicated in dark gray and black, respectively. The band gaps are shaded in gray.

can formally be divided into three groups. The first group is composed of the projections of imaginary parts of the viscoelastic bands originating from propagating elastic modes. As the imaginary components for these modes are small, the curves are located close the vertical  $\Gamma$  axis, on the left. The second set of additional curves appears due to the coupling between complex-valued evanescent modes and attenuating propagating modes located close to the  $\text{Re } k^*$  plane. These modes have small real values of  $k^*$  and occur close to the vertical  $\Gamma$  and  $X$  axes in the  $\text{Re } k^*$  plane. The third set of the additional bands originates from the requirement on continuity of dispersion curves with respect to frequency. Namely, every curve should span the full frequency range, from zero to infinity.<sup>[70,71]</sup> The mentioned bands link evanescent modes to the zero-frequency plane. Note that all “additional” bands are poorly predicted (if at all) by simple viscoelastic models as a single viscosity parameter enables only to shift dispersion bands along the frequency axis,<sup>[26,30]</sup> while more complicated behavior due to multi-mode energy dissipation cannot be captured. This highlights the importance of multi-mode viscoelastic models to correctly predict the wave dispersion in dissipative phononic materials.

To verify the validity of the observed viscoelastic effects at other frequencies, we calculated the dispersion diagrams for Large-cross unit cell made of a viscoelastic epoxy (Figures A13b and A14b). The curve trends in Figure 6c and Figure A14b, Supporting Information are similar considering the differences originating from the plate geometries discussed above. Concurrently, the viscoelastic effects are even more pronounced for the Large-cross plate. In particular, there exists a larger number of “additional” bands in the low-frequency range, governed by the multi-mode energy dissipation.

Therefore, identical phononic patterns inducing Bragg scattering result in similar or even identical (when losses are negligible) dispersion characteristics at broad frequencies. The non-dimensional analysis allows to separate the material and geometric dispersion effects enabling a straightforward comparison of dispersion bands even for viscoelastic media, when the material dispersion is coupled to geometric features.

#### 4.2.2. Local Resonances

We finally analyze the wave dispersion induced by local resonances and viscoelastic losses. Figure 7a presents a dispersion diagram for propagating waves in the elastic Spiral plate for  $E = E_{el}$ , that is, the value of  $E'$  within the band gap (Figure 4a). The narrow band gap (shaded in gray) is generated at deep sub-wavelength frequencies around  $f^* = 7.5e-3$  due to resonant vibrations of the spiral resonators (the bottom inset). Note that in-plane (blue) and out-of-plane (red) modes are fully decoupled in the considered frequency range. For a stiffer plate with  $E = E_g$ , the structure of the dispersion diagram for the propagating modes is fully preserved (cf. light-gray curves Figure 7a and bands for  $\Gamma X$  direction in Figure 7b or Figures A20 and A21, Supporting Information).

In the complete diagrams, the trends of evanescent modes (Figure 7b and Figure A15, Supporting Information) are very different from those for the cruciform pattern (Figure 6b), which can be explained by a different nature of the locally resonant and Bragg band gaps. The signature of a locally resonant band gap is the presence of a large number of almost flat modes with (close to) zero group velocity suggesting strong energy localization. These flat bands are poorly resolved in Figure 7b because the employed solution procedure fails in evaluating multiple  $k$  at a fixed frequency.<sup>[25,26,32]</sup> The same features can be found in the dispersion diagram of a plate with epoxy-coated inclusions that also has a locally-resonant band gap (Figure A22, Supporting Information and ref. [58]).

Viscoelastic losses dramatically change the overall structure of the bands (cf. Figure 7c,b) due to strong coupling between different types of modes. Nevertheless, one can observe similar viscoelastic effects as found for the viscoelastic Bragg scattering (Section 4.2.1). Namely, more involute trends of the bands also result in “smearing out” of the band-gap bounds. Further, the occurrence of a large number of “additional” bands not only governs the multi-mode energy dissipation, but also substantially changes the structure of the dispersion spectrum. An additional viscoelastic effect, not typical for the Bragg scattering, is the transformation of the flat real-valued bands (in the elastic case) into spiral-shaped inherently

complex bands (see Figure A15b, Supporting Information). The same behavior was observed previously for phononic materials with viscoelastic coated inclusions,<sup>[26]</sup> and can thus be considered a distinctive feature of local resonances in a viscoelastic medium.

Note that the mentioned viscoelastic effects on the wave dispersion driven by local resonances are relevant not only to the rheologically-complex epoxy. The band diagrams for the Spiral unit cells made of viscoelastic PMMA (not shown) are very similar to those discussed above. This reveals that the interplay between the geometric and material dispersion is general and can be expected for any dissipative polymer, regardless of its chemical structure.

## 5. Conclusion

This work presents a comprehensive analysis of the influence of material and mechanical properties of two commonly used polymers on the phononic plates dynamics, the consideration of which is often either (over)simplified or not validated experimentally. By analyzing several phononic architectures with two key wave control mechanisms at different frequency ranges, we show that this influence cannot be neglected for any combination of geometric and physical parameters of the plates, and must be taken into account to adequately predict the plate dynamics. This claim is validated by experimental tests over broad frequency ranges.

We have investigated dissipative phononic materials made of both thermoplastic and thermoset polymers and discussed the effect of viscoelasticity on their dynamics driven by the two wave scattering mechanisms—Bragg scattering and local resonances. In particular, we have conducted a combined experimental-numerical study allowing to identify the cases when simplified material models are unable to reliably predict the dynamic behavior of a phononic medium, so that a full viscoelastic modeling is necessary. The full modeling includes experimental characterization of the frequency-dependent characteristics of constituent materials (in our cases, PMMA and epoxy resin) in order to derive master curves for target frequencies, followed by the proposed fitting procedure to determine the parameters of multi-mode mechanical models approximating the material relaxation. These multi-mode models reproduce viscoelastic properties in finite element simulations that enable estimating dispersion and transmission spectra for phononic plates of any architecture, with band gaps in wide frequency ranges. The applicability of both elastic and viscoelastic simulations has been verified by comparisons of numerical predictions with experimental transmission measurements on ad-hoc fabricated specimens.

Our results indicate that the wave dynamics, and hence band gaps, strongly depend on the material relaxation spectrum governed by the main and the secondary transition zones of polymers. In the case of rheologically simple polymers, such as PMMA, a linear elastic model can correctly approximate the location and the width of Bragg band gaps induced by non-resonant scattering when viscous losses are small. However, in the presence of thin architectural elements subject to local resonances, the influence of material losses is amplified, making

elastic or simple viscoelastic models unreliable. In this case, only multi-parameter models reproducing experimental master curves can correctly capture the dynamic response.

For rheologically complex polymers, such as our epoxy resin, linear elastic, or one-parameter viscoelastic models cannot reproduce the real dynamics of phononic plates. Multimode models can predict the frequencies and width of band-gaps provided viscous losses are reproduced correctly, which may require measurements of relaxation parameters under isothermal conditions due to the inapplicability of the TTS principle.

Overall, this work provides a solid foundation for future developments in the field of viscoelastic phononics. The obtained results can be useful, for example, to correlate dynamic and mechanical properties of phononic materials with their dielectric, thermal, magnetic, and other characteristics.<sup>[72]</sup> In addition to the formulated guidelines on how to perform the viscoelastic analysis of phononic media, our findings can also be useful for other problems related to, for example, temperature-dependent or nonlinear dynamics of polymer phononics, nonlinear viscoelastic materials, pores-induced damping in additively manufactured materials, etc. Besides, our results provide a platform for developing tunable and shape-morphing phononic materials sensitive to temperature, humidity, etc.<sup>[73–75]</sup>

## Supporting Information

Supporting Information is available from the Wiley Online Library or from the author.

## Acknowledgements

A.O.K. and M.A. were supported by start-up packages from the Faculty of Science and Engineering at the University of Groningen. A.S.G., N.M.P., and F.B. were supported by the European Commission under the FET Open (“Boheme”) grant N. 863179. The authors are sincerely thankful to Prof. Katja Loos and Albert J.J. Woortman (ENTEG, the University of Groningen, the Netherlands) for the GPC analysis of PMMA and to Prof. M. Sangermano for the support in specimen preparation.

## Conflict of Interest

The authors declare no conflict of interest.

## Data Availability Statement

The data that support the findings of this study are available from the corresponding author upon reasonable request.

## Keywords

damping, phononic material, viscoelastic polymer, wave dynamics

Received: April 10, 2021

Revised: May 1, 2021

Published online:

- [1] R. Craster, S. Guenneau, *Acoustic Metamaterials: Negative Refraction, Imaging, Lensing and Cloaking*, Springer, Berlin **2013**.
- [2] P. Deymier, in *Acoustic metamaterials and Phononic Crystals*, Springer, Berlin **2013**, pp. 1–12.
- [3] V. Hahn, P. Kiefer, T. Frenzel, J. Qu, E. Blasco, C. Barner-Kowollik, M. Wegener, *Adv. Funct. Mater.* **2020**, *30*, 1907795.
- [4] Z. Liu, X. Zhang, Y. Mao, Y. Zhu, Z. Yang, C. Chan, P. Sheng, *Science* **2000**, *289*, 1734
- [5] V. Romero-García, G. Theocharis, O. Richoux, A. Merkel, V. Tournat, V. Pagneux, *Sci. Rep.* **2016**, *6*, 19519.
- [6] N. Kaina, F. Lemoult, M. Fink, G. Lerosey, *Nature* **2015**, *525*, 77.
- [7] L. Zigoneanu, B.-I. Popa, S. Cummer, *Nat. Mater.* **2014**, *13*, 352.
- [8] J. Pendry, *Phys. Rev. Lett.* **2000**, *85*, 3966.
- [9] A. Krushynska, N. Anerao, M. Badillo-Avila, M. Stokroos, M. Acuatla, *Mater. Des.* **2021**, *205*, 109714.
- [10] A. Gliozzi, M. Miniaci, A. Krushynska, B. Morvan, M. Scalerandi, N. Pugno, F. Bosia, *Sci. Rep.* **2019**, *9*, 9560.
- [11] X. Zhang, M. Xiao, Y. Cheng, M.-H. Lu, J. Christensen, *Commun. Phys.* **2018**, *1*, 97.
- [12] W. Cheng, J. Wang, U. Jonas, G. Fytas, N. Stefanou, *Nat. Mater.* **2006**, *5*, 830.
- [13] M. Hussein, C.-N. Tsai, H. Honarvar, *Adv. Funct. Mater.* **2020**, *30*, 2070047.
- [14] S. Cummer, J. Christensen, A. Alù, *Nat. Rev. Mater.* **2016**, *1*, 16001.
- [15] M. Kadic, G. Milton, M. van Hecke, M. Wegener, *Nat. Rev. Phys.* **2019**, *1*, 198.
- [16] H. Liu, Q. Zhang, K. Zhang, G. Hu, H. Duan, *Adv. Sci.* **2019**, *6*, 1900401.
- [17] M. Miniaci, A. Krushynska, A. Gliozzi, N. Kherraz, F. Bosia, N. Pugno, *Phys. Rev. Appl.* **2018**, *10*, 024012.
- [18] G. Zhu, N. Swintek, S. Wu, J. Zhang, H. Pan, J. Bass, P. Deymier, D. Banerjee, K. Yano, *Phys. Rev. B* **2013**, *88*, 144307.
- [19] S. Brûlé, E. Javelaud, S. Enoch, S. Guenneau, *Phys. Rev. Lett.* **2014**, *112*, 133901.
- [20] D. Colquitt, A. Colombi, R. Craster, P. Roux, S. Guenneau, *J. Mech. Phys. Solids* **2017**, *99*, 379.
- [21] S. Krödel, N. Thomé, C. Daraio, *Extreme Mech. Lett.* **2017**, *4*, 111.
- [22] M. Barnhart, X. Xu, Y. Chen, J. Song, G. Huang, *J. Sound Vib.* **2018**, *438*, 1.
- [23] F. Casadei, M. Ruzzene, L. Dozio, K. Cunefare, *Smart Mater. Struct.* **2009**, *19*, 015002.
- [24] G. Ma, P. Sheng, *Sci. Adv.* **2016**, *2*, e1501595.
- [25] K. Matlack, A. Bauhofer, S. Krödel, A. Palermo, C. Daraio, *Proc. Natl. Acad. Sci. U. S. A.* **2016**, *113*, 8386.
- [26] A. Krushynska, V. Kouznetsova, M. Geers, *J. Mech. Phys. Solids* **2016**, *96*, 29.
- [27] L. D'Alessandro, A. Krushynska, R. Ardito, N. Pugno, A. Corigliano, *Sci. Rep.* **2020**, *10*, 16403.
- [28] S. J. Mitchell, A. Pandolfi, M. Ortiz, *J. Mech. Phys. Solids* **2014**, *65*, 69.
- [29] E. Manconi, B. Mace, *J. Sound Vib.* **2010**, *329*, 3928.
- [30] R. Moiseyenko, V. Laude, *Phys. Rev. B* **2011**, *83*, 064301.
- [31] F. Farzbod, M. Leamy, *J. Vib. Acoust.* **2011**, *133*, 051010.
- [32] E. Andreassen, J. Jensen, *J. Vib. Acoust.* **2013**, *135*, 041015.
- [33] J. Manimala, C. Sun, *J. Appl. Phys.* **2014**, *115*, 023518.
- [34] Y. Chen, M. Barnhart, J. Chen, G. Hu, C. Sun, G. Huang, *Comp. Struct.* **2016**, *136*, 358.
- [35] L. Van Belle, C. Claeys, E. Deckers, W. Desmet, *J. Sound Vib.* **2017**, *409*, 1.
- [36] B. Merheb, P. A. Deymier, M. Jain, M. Alohyna-Lesuffleur, S. Mohanty, A. Berker, R. Greger, *J. Appl. Phys.* **2008**, *104*, 064913.
- [37] T.-T. Wang, V. Laude, M. Kadic, Y. Wang, Y.-S. Wang, *Appl. Sci.* **2019**, *9*, 2825.
- [38] B. Clements, *J. Appl. Phys.* **2012**, *112*, 083511.
- [39] J. Vincent, *Structural Biomaterials*, Princeton University Press, Princeton **2012**.
- [40] J. Ferry, *Viscoelastic Properties of Polymers*, Wiley, New York **1980**.
- [41] R. S. Lakes, *Viscoelastic Materials*, Cambridge University Press, New York **2009**.
- [42] S. H. Crandall, *J. Sound Vib.* **1970**, *11*, 3.
- [43] C. Federico, J. Bouvard, C. Combeaud, N. Billon, *Polymer* **2018**, *139*, 177.
- [44] M. Aoki, A. Shundo, S. Yamamoto, K. Tanaka, *Soft Matter* **2020**, *16*, 7470.
- [45] J. Feng, Z. Guo, *Composites, Part B* **2016**, *85*, 161.
- [46] C. Gracia-Fernández, S. Gómez-Barreiro, J. López-Beceiro, J. Tarrío Saavedra, S. Naya, R. Artiaga, *Polym. Test.* **2010**, *29*, 1002.
- [47] C. Hall, *Polymer Materials*, Macmillan & Co., New York **1989**.
- [48] J. Y. Jho, A. Yee, *Macromolecules* **1991**, *24*, 1905.
- [49] M. Nasraoui, P. Forquin, L. Siad, A. Rusinek, *Mater. Des.* **2012**, *37*, 500.
- [50] L. Gibson, M. Ashby, *Cellular Solids: Structure and Properties*, Pergamon Press, Oxford **1988**.
- [51] A. F. Yee, M. T. Takemori, *J. Polym. Sci., Polym. Phys. Ed.* **1982**, *20*, 205.
- [52] B. Read, *Polymer* **1981**, *22*, 1580.
- [53] J. Capodagli, R. Lakes, *Rheol. Acta* **2008**, *47*, 777.
- [54] D. O'Brien, P. Mather, S. White, *J. Compos. Mater.* **2001**, *35*, 883.
- [55] Y. He, *Thermochim. Acta* **2005**, *436*, 127.
- [56] J. Diani, P. Gilormini, C. Frédy, I. Rousseau, *Int. J. Solids Struct.* **2012**, *49*, 793.
- [57] S. Saseendran, M. Wysocki, J. Varna, *Adv. Manuf.: Polym. Compos. Sci.* **2016**, *2*, 74.
- [58] A. Krushynska, V. Kouznetsova, M. Geers, *J. Mech. Phys. Solids* **2014**, *71*, 179.
- [59] F. González-García, B. Soares, V. J. R. R. Pita, R. Sánchez, J. Rieumont, *J. Appl. Polym. Sci.* **2007**, *106*, 2047.
- [60] Y. Shangguan, F. Chen, E. Jia, Y. Lin, J. Hu, Q. Zheng, *Polymers* **2017**, *9*, 567.
- [61] M. Mangion, G. Johari, *J. Polym. Sci., Part B: Polym. Phys.* **1990**, *28*, 71.
- [62] D. Mead, *J. Sound Vib.* **1973**, *27*, 235.
- [63] J. Weese, *Comput. Phys. Commun.* **1993**, *77*, 429.
- [64] T. Kolda, R. M. Lewis, V. Torczon, *SIAM Rev.* **2003**, *45*, 385.
- [65] A. Foehr, O. R. Bilal, S. D. Huber, C. Daraio, *Phys. Rev. Lett.* **2018**, *120*, 205501.
- [66] C. Goffaux, J. Sánchez-Dehesa, A. Levy Yeyati, P. Lambin, A. Khelif, J. Vasseur, B. Djafari-Rouhani, *Phys. Rev. Lett.* **2002**, *88*, 225502.
- [67] B. Yuan, V. Humphrey, J. Wena, X. Wen, *Ultrasonics* **2013**, *53*, 1332.
- [68] M. S. Kushwaha, P. Halevi, L. Dobrzynski, B. Djafari-Rouhani, *Phys. Rev. Lett.* **1993**, *71*, 2022.
- [69] N. Kaina, M. Fink, G. Lerosey, *Sci. Rep.* **2013**, *3*, 3240.
- [70] A. Krushynska, V. Meleshko, *J. Acoust. Soc. Am.* **2011**, *129*, 1324.
- [71] R. D. Mindlin, *An Introduction to the Mathematical Theory of Vibrations of Elastic Plates*, World Scientific, Singapore **2007**.
- [72] T. Still, W. Cheng, M. Retsch, R. Sainidou, J. Wang, U. Jonas, N. Stefanou, G. Fytas, *Phys. Rev. Lett.* **2008**, *100*, 194301.
- [73] K. O. M. Billon, E. Sadoulet-Reboul, M. Collet, P. Butaud, G. Chevallier, A. Khelif, *Smart Mater. Struct.* **2019**, *28*, 035007.
- [74] Z. Li, Y. Li, S. Kumar, H. Lee, *J. Appl. Phys.* **2019**, *126*, 155102.
- [75] P. Butaud, D. Renault, B. Verdin, M. Ouisse, G. Chevallier, *Smart Mater. Struct.* **2020**, *29*, 065002.

# ADVANCED FUNCTIONAL MATERIALS

## Supporting Information

for *Adv. Funct. Mater.*, DOI: 10.1002/adfm.202103424

### Dissipative Dynamics of Polymer Phononic Materials

*Anastasiia O. Krushynska,\* Antonio S. Gliozzi, Alberto Fina, Dmitry Krushinsky, Daniele Battezzore, Miguel A. Badillo-Ávila, Mónica Acuautla, Stefano Stassi, Camilla Noè, Nicola M. Pugno, and Federico Bosia*

# Supplementary information for

## Dissipative dynamics of polymer phononic materials

Anastasiia O. Krushynska<sup>\*1</sup>, Antonio S. Gliozzi<sup>2</sup>, Alberto Fina<sup>2</sup>, Dmitry Krushinsky<sup>3</sup>, Daniele Battegazzore<sup>2</sup>, Miguel A. Badillo-Avila<sup>1</sup>, Mónica Acuautla<sup>1</sup>, Stefano Stassi<sup>2</sup>, Camilla Noè<sup>2</sup>, Marco Scalerandi<sup>2</sup>, Nicola M. Pugno<sup>4,5</sup>, Federico Bosia<sup>2</sup>

<sup>1</sup>*Engineering and Technology Institute Groningen (ENTEG), Faculty of Science and Engineering, University of Groningen, Nijenborgh 4, 9747AG Groningen, The Netherlands*

<sup>2</sup>*Department of Applied Science and Technology, Politecnico di Torino, Corso Duca degli Abruzzi 24, 10124 Torino, Italy*

<sup>3</sup>*Operations Research and Logistics Group, Wageningen University & Research, Hollandseweg 1, 6706 KN Wageningen, The Netherlands*

<sup>4</sup>*Laboratory of Bio-inspired, Bionic, Nano, Meta Materials & Mechanics, Department of Civil, Environmental and Mechanical Engineering, University of Trento, Via Mesiano, 77, 38123 Trento, Italy*

<sup>5</sup>*School of Engineering and Materials Science, Queen Mary University of London, Mile End Road, London E1 4NS, UK*

Correspondence and requests for materials should be addressed to A.O.K. ([a.o.krushynska@rug.nl](mailto:a.o.krushynska@rug.nl))

### Table of Contents

A1. Materials manufacturing, characterization and methods .....	2
A1.1 Fourier Transform Infrared Spectrometry (FTIR) .....	2
A1.2 Gel permeation chromatography (GPC) .....	3
A1.3 Epoxy synthesis .....	4
A1.4 Swelling tests .....	5
A1.5 Scanning Electron Microscopy (SEM) .....	6
A1.6 Differential Scanning Calorimetry (DSC) coupled with thermogravimetric (TGA) analysis .....	6
A1.7 Dynamic mechanical thermal analysis (DMTA) .....	7
A2 Viscoelasticity of polymers .....	10
A2.1 Mathematical treatment of viscoelasticity .....	10
A2.2 Estimation of the storage glass modulus .....	11
A2.3 LNL technique for fitting master curves .....	12
A2.3.1 Optimizing $E$ .....	12
A2.3.2 Optimizing $\tau$ .....	14
A2.3.3 Implementation details .....	14
A2.3.4 Coefficients of the Prony series .....	15

A3 Phononic plates.....	16
A3.1 Geometry of the samples .....	16
A3.2 Experimental measurements of the wave transmission .....	17
A3.3 Numerical analysis .....	17
A3.3.1 Transmission analysis.....	17
A3.3.2 Dispersion analysis.....	17
Supplementary References .....	24

## A1. Materials manufacturing, characterization and methods

### A1.1 Fourier Transform Infrared Spectrometry (FTIR)

The FTIR analysis was performed on a PerkinElmer Frontier spectrometer on the PMMA used in this work and compared with a “standard” PMMA from our internal database. The spectra (transmittance vs. wavenumber) for the two materials are shown in Figure A1. The materials have almost identical signals for C-H stretching peaks (region I) and the C=O peak (region III). The fingerprint (region IV) of the used PMMA is also identical to the reference PMMA. Therefore, the data convincingly confirm that the commercial material is indeed a neat PMMA.

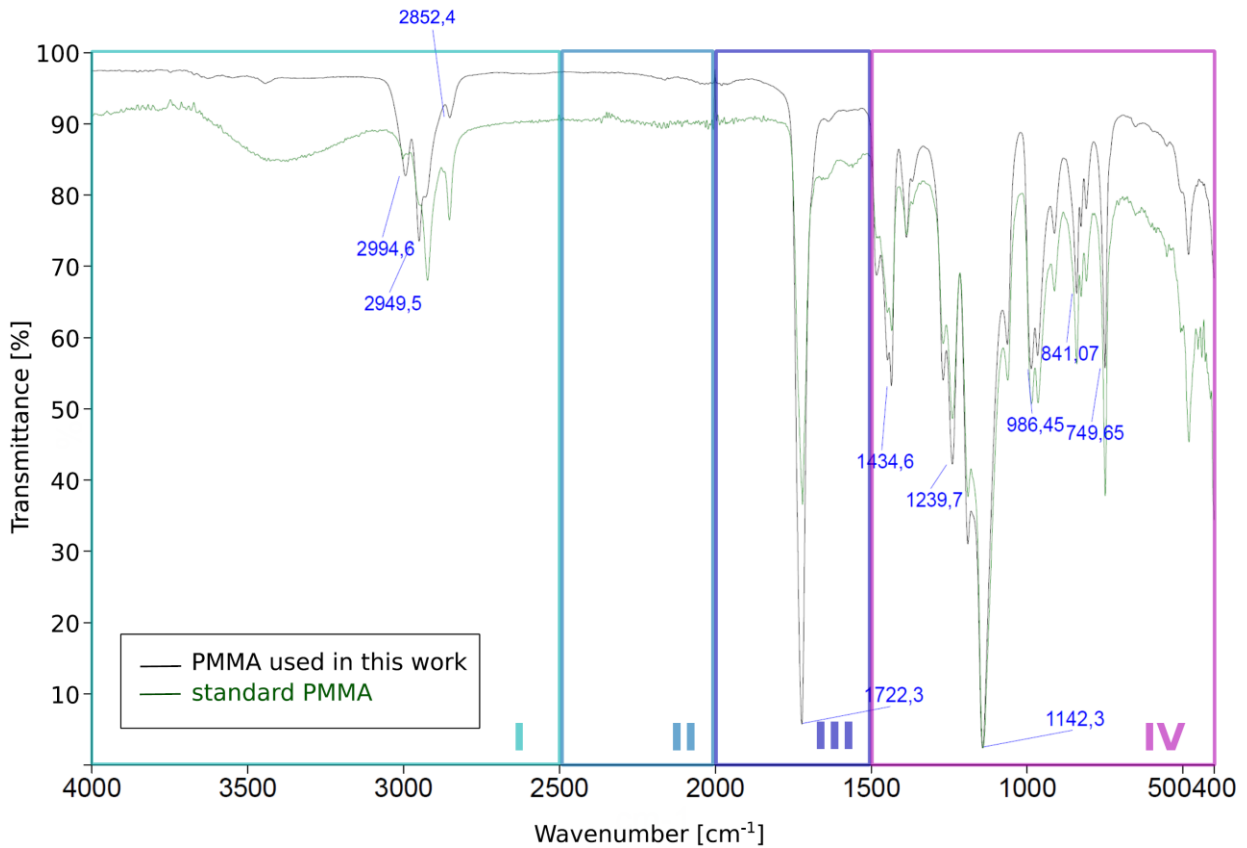


Figure A1. The FTIR spectrum of the commercial material vs. standard PMMA.

## A1.2 Gel permeation chromatography (GPC)

The GPC of the PMMA was performed in DMF (containing 0.01 M LiBr) on a Viscotek GPC max equipped with model 302 TDA detectors, two columns (Agilent Technologies-PolarGel-L and M, 8 $\mu$ m 30cm) at a flow rate of 1.0 ml/min. The columns and detectors were held at 50°C. The samples were filtered over a 0.2  $\mu$ m PTFE filter prior to injection.

Data acquisition and calculations were performed using Viscotek OmniSec software version 5.0. Molecular weights were determined based on a conventional calibration curve generated from narrow dispersity PMMA standards (Agilent and PS, Mw from 550 to 1190000 g/mol, Figure A2).

The measured molecular weight  $M_w^{(p)}$  is 1474 kg/mol and molar number  $M_n^{(p)}$  is 344.7 kg/mol (here the superscript in brackets refers to PMMA). Since these values are at the column separation and slightly larger than the available highest MW PMMA standard, the results were also re-evaluated based on light scattering techniques, independent of standards (Figure A3). The derived values  $M_w^{(p)} = 1444$  kg/mol and  $M_n^{(p)} = 275.13$  kg/mol are consistent with the previous measurements.

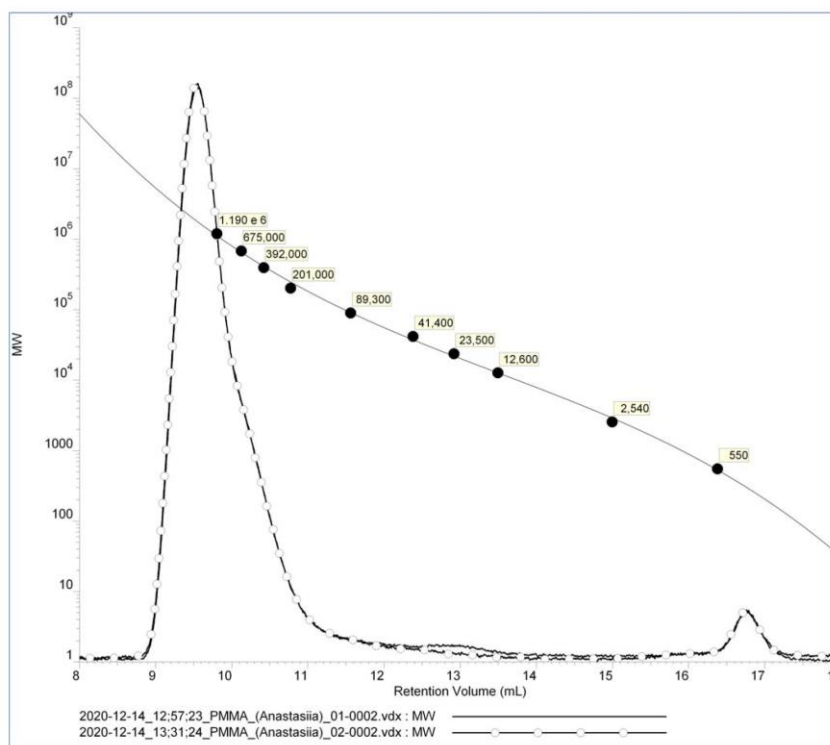


Figure A2. Overlay report conventional calibration (DMF system).



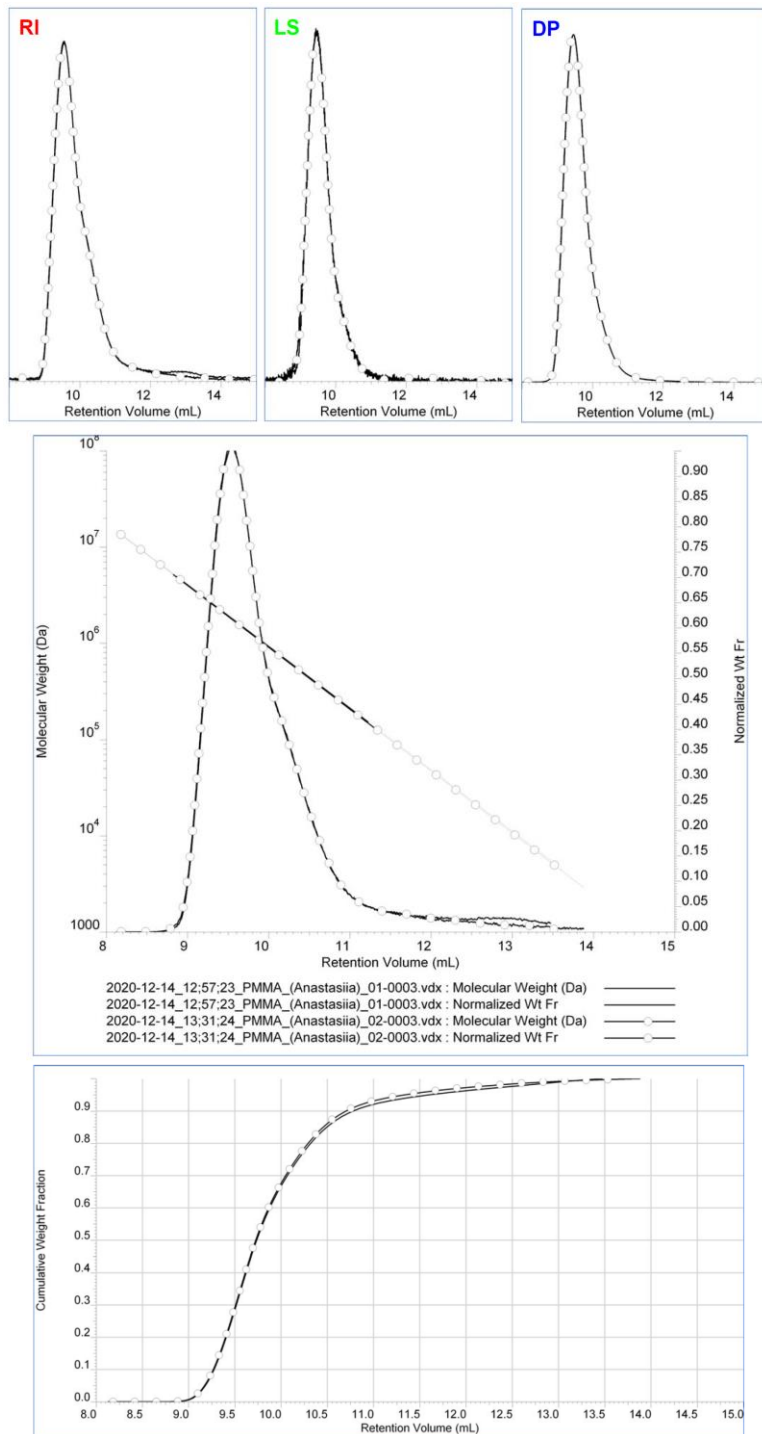


Figure A3. Overlay report LS, triple detection (DMF system).

### A1.3 Epoxy synthesis

Epoxy plates of various thicknesses were synthesized from bisphenol-A-diglycidyl ether (DGEBA from Aldrich,  $M_w=340.41$  g/mol) and the amine tetraethylpentamine (TEPA from Aldrich,  $M_w=189.302$

g/mol) following the procedure reported in Ref. [1]. Specifically, the epoxy resin DGEBA was mixed with 20 phr (per hundred resin) of TEPA. The two reagents were then stirred for 5 minutes to obtain a homogeneous mixture and degassed for 10 minutes. Next, the formulation was poured into a mold and cured for 2 h at 80 °C. Afterwards, the cross-linked samples were subjected to a post-curing treatment at 150 °C for 30 min.

The molecular weight between the cross-linking points was calculated by means of the equation:

$$M_c = (m_a + 2m_e)/3, \quad (S1.1)$$

where  $m_a$ ,  $m_e$  are the molecular weights of the amine and epoxide monomers [2]. The estimated value of 290.04 g/mol excellently agrees with that for the DGEBA/TEPA epoxy [3].

#### A1.4 Swelling tests

A portion of the cured epoxy resin was cut to carry out a swelling test. THF is usually reported as the most common solvent for epoxy. Nevertheless, as it poses a risk of explosion, we have employed dichloromethane (which also presents good solvent properties) as a substitute solvent for the swelling tests. An epoxy sample of mass of 0.3132 g was immersed in dichloromethane for a day. During the day, the piece was extracted, lightly dried with lint-free tissue paper, weighed, and returned to the solvent. The process was repeated several times. The expansion of the sample (swelling) is depicted in Figure A4. It was found that the largest increase in swelling happens in less than 5 hours. Nevertheless, the expansion of the block only achieves a 17.2 % increase after 24 hours. This means that the epoxy resin is compact and well-cured.

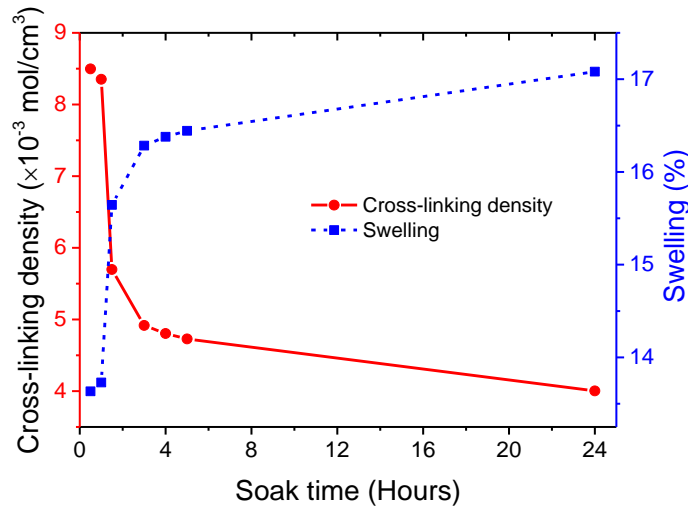


Figure A4. Swelling percentage and cross-linking density of the cured epoxy.

An estimation of the cross-linking density was made following the Flory-Huggins theory [4]. A density of  $\rho_2 = 1.1$  g/ml was calculated for the epoxy resin by volume displacement. Because we used dichloromethane instead of THF, the value change of some parameters was considered. The density and molar volume of dichloromethane were taken as  $\rho_1 = 1.33$  g/ml and  $V_1 = 64$  cm<sup>3</sup>/mol [5]. The Flory-Huggins interaction parameter at a volume fraction of  $\phi_2 = 0$  was set to  $\chi = 1$ . The decision was made on the basis of the poor swelling effect that dichloromethane had with our epoxy resin, as also reported in Ref. [5]. After 24 hours, the cross-linking density was estimated as  $\nu = 4 \times 10^{-3}$  mol/cm<sup>3</sup>, which is a larger number in comparison to that in Ref. [4]. This can be directly attributed to the high curing (80 °C) and

post-curing temperatures (150 °C) for our material, which caused the high crosslinking in the cured epoxy. In the following sections this will also be corroborated by the DSC and DMTA results.

### A1.5 Scanning Electron Microscopy (SEM)

Small chunks of material were cut off from the epoxy plate and the inner section was analyzed under scanning electron microscopy (SEM). For SEM imaging, the samples were sputtered with 5 nm of gold and measured at high vacuum under an acceleration voltage of 10 kV.

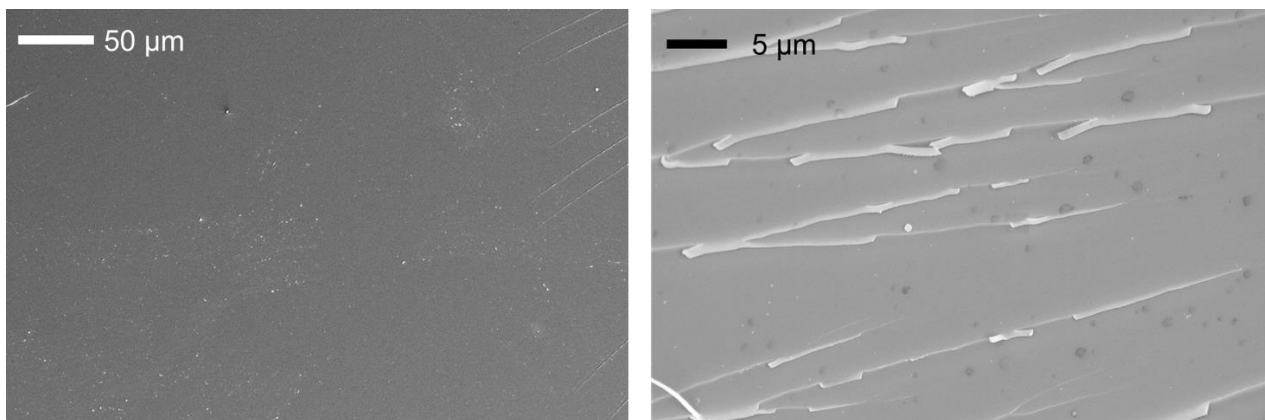


Figure A5. Cross-section morphology of *epoxy*.

In Figure A5 (left), the epoxy cross section shows a dense, uniform nature without major discontinuities. The small white particles are residues, and the white wrinkles are fracture lines formed from the cutting procedure. At a closer look (Figure A5, right), a series of small pockets of air is featured. However, the air bubbles appear in random regions of the resin and thus they are not representative of the whole polymer. The few air pockets were probably formed during the molding process of the epoxy resin.

### A1.6 Differential Scanning Calorimetry (DSC) coupled with thermogravimetric (TGA) analysis

To get a deeper insight into the quality and temperature-dependent characteristics of the epoxy, we performed a DSC/TGA analysis. Similar data for a commercial PMMA can be found elsewhere [6, 7].

For the DSC/TGA analysis, 16 mg of the cured epoxy were heated from room temperature to 275°C at a heat rate of 10 °C/min under argon ambiance at 100 ml/min. Figure S6 shows that mass loss during heating is only 1.5 %. Most likely, adsorbed water and other trace substances were lost by evaporation. Also, the small loss means that no precursors remained trapped, thus giving the resin a good, dense quality.

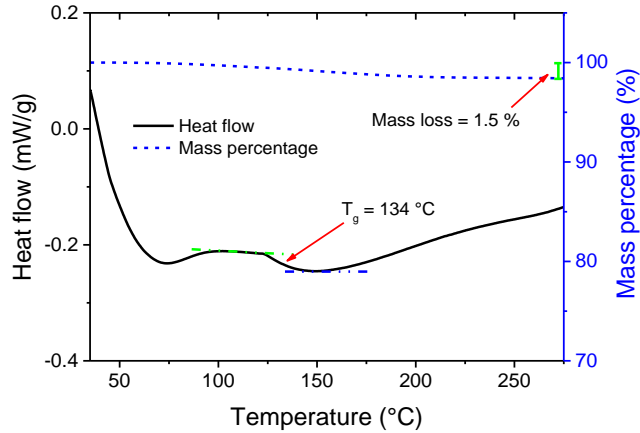


Figure A6. TGA/DSC thermograms for cured epoxy.

From Figure A6, the midpoint  $T_g$  estimated for the cured epoxy is 134 °C, which is a slightly lower than that from DMTA analysis. This can be explained by the fact that DSC is sensitive to variations of the heat capacity, while the DMA measures mechanical relaxation governed by the excitation frequency [8]. The large  $T_g$  of the cured epoxy is an indication of high cross-linking due to high processing temperatures during curing.

### A1.7 Dynamic mechanical thermal analysis (DMTA)

The DMTA analysis was performed by means of a Q800 by TA Instrument (USA) on a single clamped cantilever configuration with a fix span length of 17.5 mm. The cross-sectional dimensions of the samples were approximately 10.0 mm x 2.9 mm for the PMMA and 10.2 mm x 2.2 mm for the epoxy.

The glass transition temperatures were determined by applying a 2°C/min temperature sweep at 0.05% strain from -80°C to 180°C for epoxy and from -60°C to 150°C for PMMA at 1 Hz. The temperature ramp diagrams are shown in Figures A7-A8. The measurements for the PMMA are in an excellent agreement with similar results in Ref. [6].

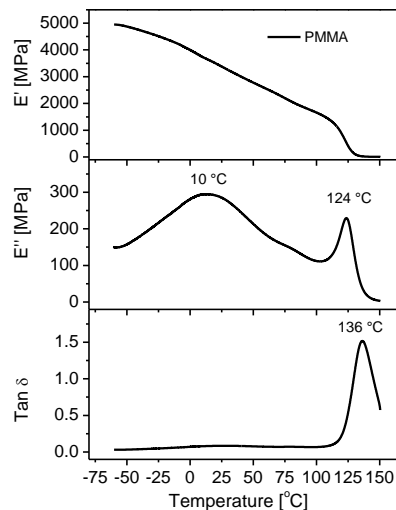


Figure A7. DTA data for PMMA for a temperature sweep at 2°C/min, 0.05% strain and 1Hz.

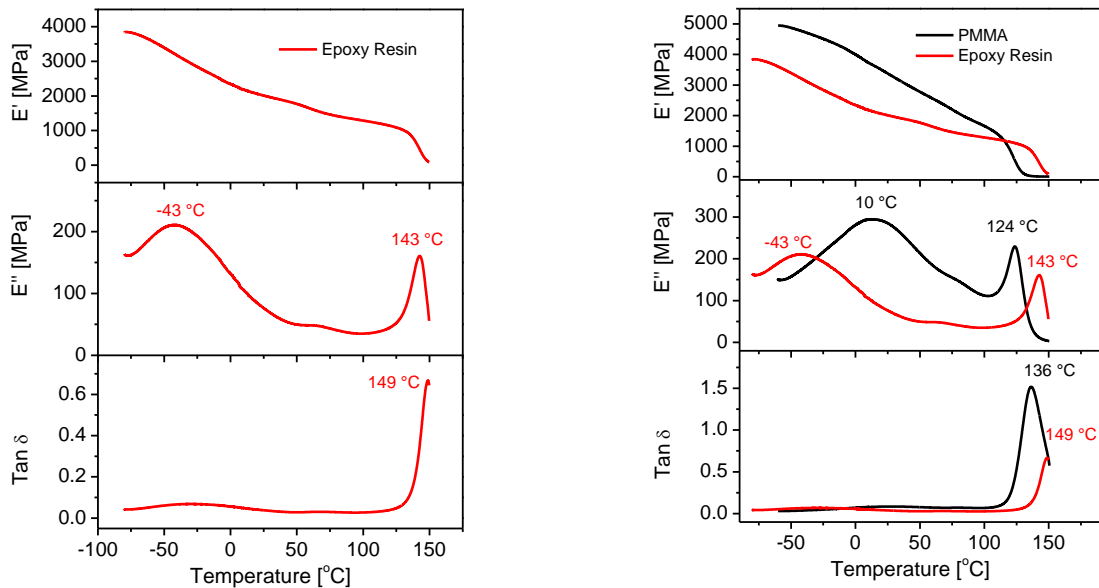


Figure A8. DTA data for **epoxy** (left) and, for comparison, **epoxy and PMMA** (right) at a temperature sweep at 2°C/min, 0.05% strain and 1Hz.

The primary ( $\alpha$ ) transition zone spans from about 100°C to 140°C for PMMA and from 110°C to above 150°C for epoxy. The local maximum of the loss factor at these frequencies approximately corresponds to the values of  $T_g$ . The secondary relaxation zones for the both polymers are discussed in the main text.

The time-dependent relaxation moduli were determined by means of frequency sweeps at 0.05% strain for the temperature gradually increasing from -25°C to 30°C (for the PMMA) and from -10°C to 30°C (for the epoxy) with increment 5°C. The measured moduli were shifted into master curves (Figures A9a, A10a) by applying the time-temperature superposition (TTS) principle.

For the PMMA, fairly good overlay  $E'$ ,  $E''$ , and  $\tan \delta_E$  plots are obtained after optimizing horizontal shifting on  $E'$  plots *vs.* frequency obtained at different temperatures (Trios software version 4 by TA Instrument), thus, confirming the validity of the TTS principle. Arrhenius fitting on shifting factors yields activation energy in the range of 100 kJ/mol that is consistent with the reported values [9, 6]. Hence, we conclude that PMMA behaves as a rheologically simple material at the analyzed frequencies.

For the epoxy, in contrast, the horizontal shift of  $E'$  plots *vs.* frequency obtained at different temperatures (Figure A10) provided an apparently reasonable curve for  $E'$  but the overlay obtained for  $E''$  and  $\tan \delta_E$  are not satisfactory. Also, fitting with Arrhenius model is not very good and the value of the activation energy appears to be rather high, as commented in the main text. The WLF equation has very high values of  $c_1$  and  $c_2$  with a poor alignment of the shift factors (Figure A10c). These experimental results prove a rheologically complex material behavior.

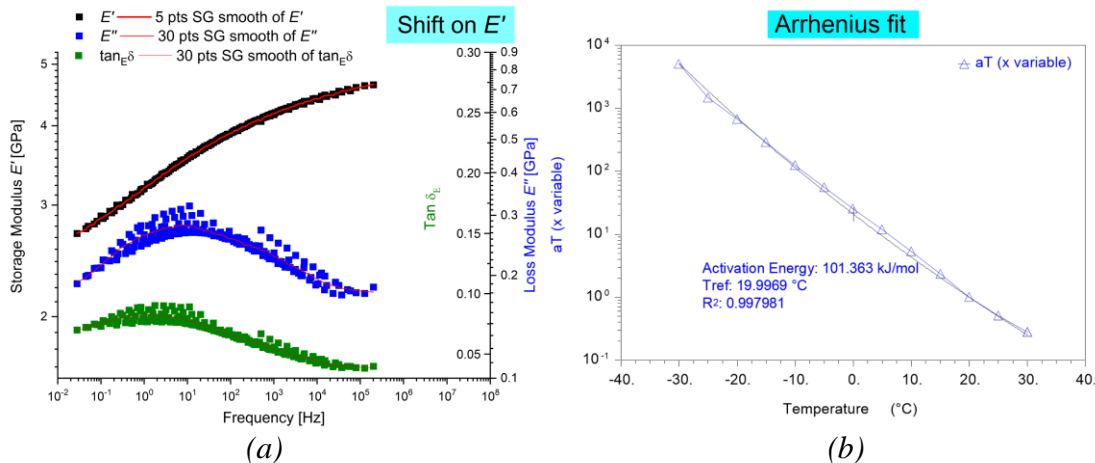


Figure A9. (a) Master curves for **PMMA** derived by means of the time-temperature superposition principle for experimental data with (b) horizontal shift factors on  $E'$  for the Arrhenius fit

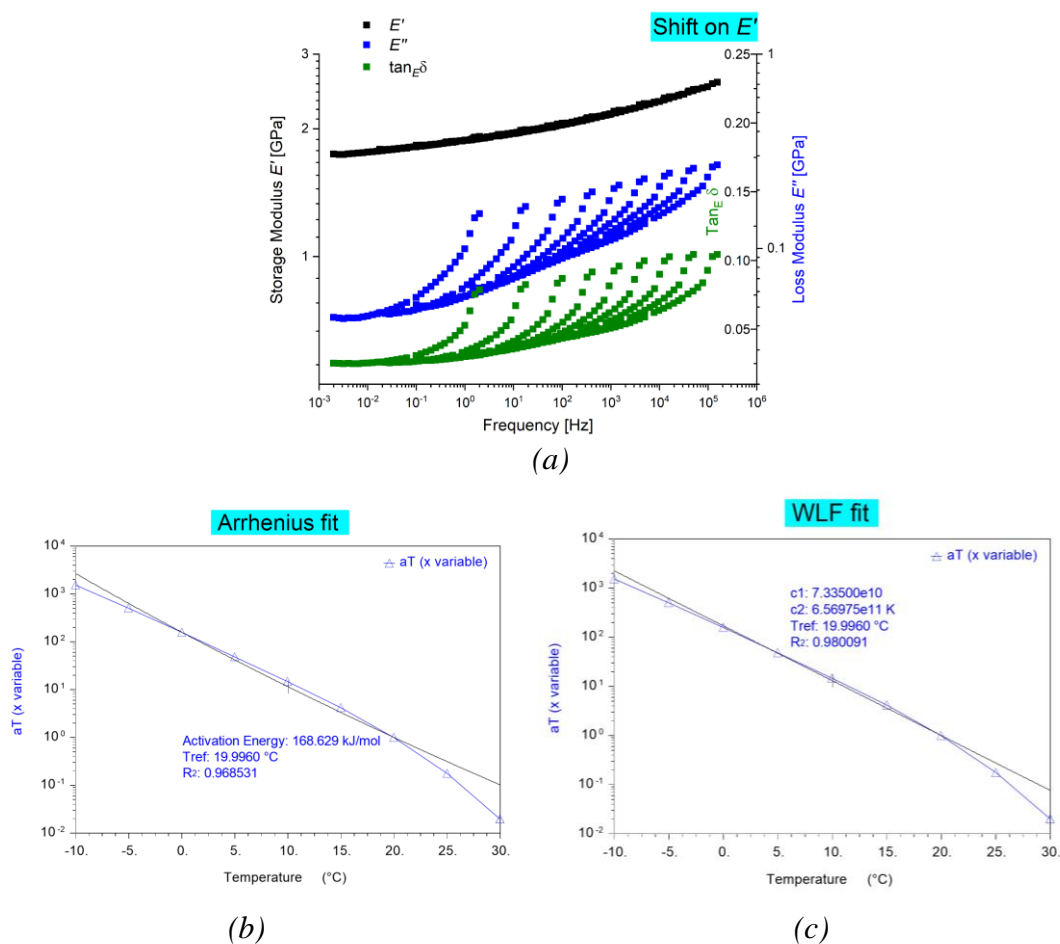


Figure A10. (a) Master curves for **epoxy** derived by means of the TTS principle for experimental data with horizontal shift factors on  $E'$  for the (b) Arrhenius and (c) WLF fits

## A2 Viscoelasticity of polymers

### A2.1 Mathematical treatment of viscoelasticity

The time required for a material to return to an equilibrium state after the application of mechanical loading – the characteristic relaxation time – can be associated with vibration modes of molecules. For neatly packed molecules, a large number of related degrees of freedom leads to a continuous distribution of relaxation time  $H(\log \tau)d(\log \tau)$  allowing to represent the relaxation modulus  $E^*(t) = E'(t) + iE''(t)$  by an integral [10]:

$$E^*(t) = E_r + \int_0^\infty H(\log \tau) \exp(-t/\tau) d(\log \tau), \quad (\text{S2.1})$$

where  $E_r$  is the equilibrium or “relaxed” modulus [10, 11]. The continuous distribution  $H(\log \tau)$  is often replaced, for simplicity, by a discrete one, under an assumption that the material response can be reproduced by mechanical spring-dashpot models [11, 12], i.e.,

$$H(\log \tau) = \sum_{n=1}^N E_n \delta(\log \tau - \log \tau_n). \quad (\text{S2.2})$$

Here,  $N$  denotes the number of Maxwell elements (a spring and a dashpot in series) or Kelvin-Voigt elements (a spring and a dash-pot in parallel) in the mechanical model,  $\delta$  is the Dirac delta function, and  $\tau$  is the ratio of the (Newtonian) viscosity of a dashpot to the stiffness of a spring. The coefficients  $E_n$  and  $\tau_n$  are discrete sets of the relaxation moduli and relaxation times, respectively. Substitution of Equation (2) into Equation (1) results, after simple mathematical transformations, in a standard Prony series [12]:

$$E^*(t) = E_r + \sum_{n=1}^N E_n \exp\left(-\frac{t}{\tau_n}\right). \quad (\text{S2.3})$$

We further proceed with discrete relaxation times, as it allows a straightforward mathematical treatment. Besides, discrete relaxation models are employed in most commercial finite-element packages.

The values of  $E_n$  and  $\tau_n$  are used to fit experimental master curves measured, e.g., by the DMTA (Section A1.7) [11]. For this, one typically specifies  $\tau_n$ ,  $n = 1, 2, \dots, N$  and estimates the corresponding values of  $E_n$  [13, 14, 12]. The limits for  $\tau_n$  are governed by available experimental data or target frequencies. In general, the values of  $\tau_n$  are arbitrary and can be represented as powers of 10, for simplicity [12]. The value of  $N$  is governed by the number of spring-dashpot elements in an adopted mechanical model. The simplest models contain a single Maxwell or Kelvin-Voigt element ( $N = 1$ ) and are known as Maxwell and Kelvin-Voigt (KV) models, respectively. The corresponding storage and loss shear moduli are:

$$E' = \frac{E_1 \omega^2 \tau_1^2}{1 + \omega^2 \tau_1^2}, \quad E'' = \frac{E_1 \omega \tau_1}{1 + \omega^2 \tau_1^2} \quad (\text{S2.4})$$

for the Maxwell model, and

$$E' = E_1, \quad E'' = \eta \omega \quad (\text{S2.5})$$

for the Kelvin-Voigt model. Here  $E_1$  is the elastic modulus of a spring,  $\eta$  is the viscosity of a dashpot, and  $\tau_1 = \eta/E_1$ .

More complex are multi-mode (generalized) models with several Maxwell or Kelvin-Voigt elements [11, 15, 12]. The generalized Maxwell model has, e.g., the following relations for the relaxation moduli:

$$E' = E_r + \sum_{n=1}^N \frac{E_n \omega^2 \tau_n^2}{1 + \omega^2 \tau_n^2}, \quad E'' = \sum_{n=1}^N \frac{E_n \omega \tau_n}{1 + \omega^2 \tau_n^2}. \quad (\text{S2.6})$$

It is important to avoid the misconception that multi-mode models are the only models capable to fit experimental data. The choice of a mechanical model is governed by its accuracy to describe the material relaxation. In fact, any model properly fitting experimental data can be a potential candidate to represent relaxation moduli of a given material. This explains why the results obtained by employing a particular model are, in general, relevant only to a specific material at certain frequencies, and can be meaningless for the same material at other frequencies or temperature or for other polymers at similar frequencies.

## A2.2 Estimation of the storage glass modulus

Ultrasound wave velocities in the polymer samples were measured by a time-domain method based on the time of flight (ToF) principle. We used two samples with dimensions 140mm x 20 mm x 2.8mm (PMMA) and 144mm x 13mm x 3mm (epoxy). The samples were covered with a reflecting tape and oriented along the trajectory of a moving head of the Laser Vibrometer (Polytec, OFV 505) as shown in Figure A11a.

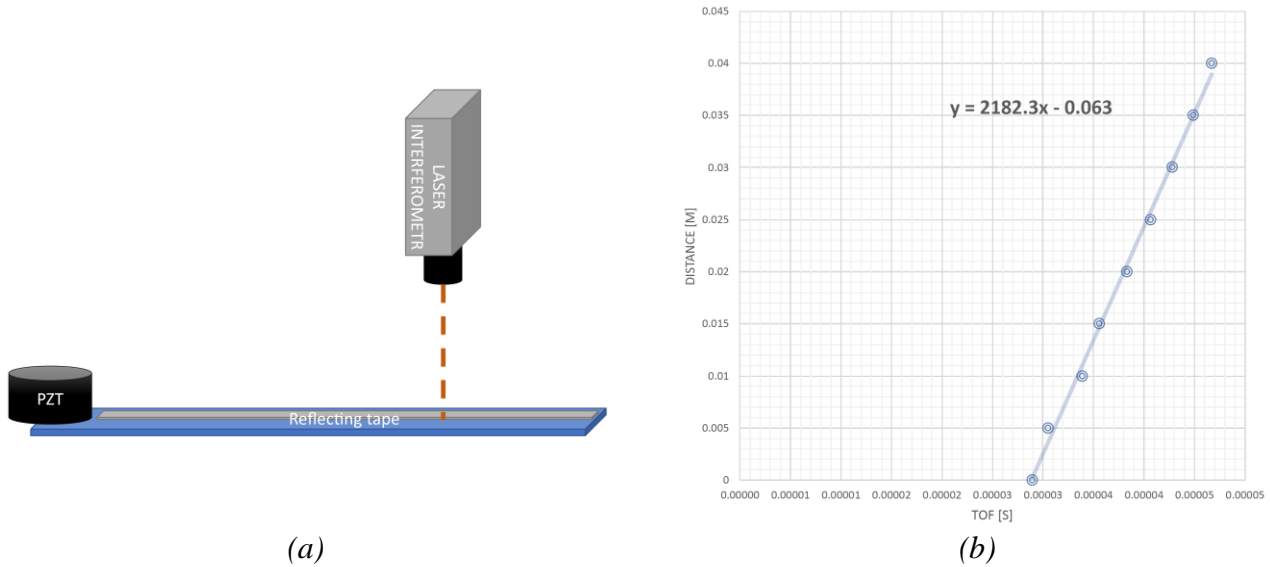


Figure A11. (a) Schematics of the ToF measurement setup; (b) time of flight of the first arrival time of a signal vs. distance for PMMA.



A narrow-band pulse centered around 200 kHz was injected by a PZT transducer placed at one end of a sample. The time of its arrival was measured at different positions along the sample. The estimated time corresponding to the ToF at each distance is plotted versus the distance in Figure A11b (for the PMMA). The slope of the fitting curve is the required ultrasonic wave velocity. This velocity is  $c_p^{(P)} = 2182$  m/s for the PMMA and  $c_p^{(E)} = 1654$  m/s for the epoxy.

The sample geometries suggest that their mechanical response can be described under the plane stress assumption. Thus, the measured velocities are the velocities of longitudinal waves in thin plates, which allows the estimation of the Young's modulus of the bulk material in the glassy state, under assumption on an isotropic behavior:

$$E_g^{(P)} = \rho \left( c_p^{(P)} \right)^2 \left( 1 - \left( \nu^{(P)} \right)^2 \right) \approx 4.91 \text{ GPa}; \quad (\text{S2.7})$$

$$E_g^{(E)} = \rho \left( c_p^{(E)} \right)^2 \left( 1 - \left( \nu^{(E)} \right)^2 \right) \approx 2.86 \text{ GPa}, \quad (\text{S2.8})$$

where  $\nu^{(P)}, \nu^{(E)}$  are Poisson's ratio of the PMMA and epoxy.

### A2.3 LNL technique for fitting master curves

Recall that we consider the problem of finding the coefficients  $\mathbf{E} = (E_n)_{n \in C}$  and  $\boldsymbol{\tau} = (\tau_n)_{n \in C}$  in the following form:

$$\min_{\mathbf{E}, \boldsymbol{\tau}} (\|F_1(\mathbf{E}, \boldsymbol{\tau}) - \mathbf{y}_1\|_2 + \alpha \|F_2(\mathbf{E}, \boldsymbol{\tau}) - \mathbf{y}_2\|_2), \quad (\text{S2.9})$$

where  $F_1$  and  $F_2$  are two vector-valued functions:

$$F_1(\mathbf{E}, \boldsymbol{\tau}) = \left( \sum_{i \in C} E_i f_1(\tau_i x_j) \right)_{j \in P}, \quad (\text{S2.10})$$

$$F_2(\mathbf{E}, \boldsymbol{\tau}) = \left( E_0 + \sum_{i \in C} E_i f_2(\tau_i x_j) \right)_{j \in P} \quad (\text{S2.11})$$

with  $f_k(x) = \frac{x^k}{1+x^2}$ ,  $k \in \{1,2\}$ . Set  $P$  enumerates the *control* points, vector  $x \in \mathbb{R}^{|P|}$  holds the  $\omega$ -values of the points, vectors  $\mathbf{y}_1$  and  $\mathbf{y}_2$  contain their  $E'$  and  $E''$  values, and set  $C$  enumerates the approximating curves. The notations  $\|\cdot\|_1$ ,  $\|\cdot\|_2$  and  $\|\cdot\|_\infty$  denote the standard  $l_1$ -,  $l_2$ - (Euclidean) and  $l_\infty$ -norms, respectively. Parameter  $\alpha$  compensates for the imbalance between the magnitude of values in  $\mathbf{y}_1$  and  $\mathbf{y}_2$ .

Let us assume for now (this assumption will be dropped later) that "good" values for  $\boldsymbol{\tau}$  are known.

#### A2.3.1 Optimizing $E$

Note that  $l_2$ -norm can be approximated by a linear combination of  $l_1$ - and  $l_\infty$ -norms. So, problem (S2.9) can be replaced by

$$\begin{aligned} & \min_{\mathbf{E}, \boldsymbol{\tau}} \beta [\|F_1(\mathbf{E}, \boldsymbol{\tau}) - \mathbf{y}_1\|_1 + \alpha \|F_2(\mathbf{E}, \boldsymbol{\tau}) - \mathbf{y}_2\|_1] \\ & + (1 - \beta) [\|F_1(\mathbf{E}, \boldsymbol{\tau}) - \mathbf{y}_1\|_\infty + \alpha \|F_2(\mathbf{E}, \boldsymbol{\tau}) - \mathbf{y}_2\|_\infty], \end{aligned} \quad (\text{S2.12})$$

where  $\beta$  is a parameter that depends only on  $|P|$ .

The advantage of this formulation is that  $l_1$ - and  $l_\infty$ -norms can be linearized. This, in turn, means that for any fixed  $\boldsymbol{\tau}$ , optimal  $\mathbf{E}$  can be efficiently found by solving the following Linear Program (LP), see, e.g., Ref. [15]:

$$\min_{\mathbf{E}} \beta w_1 + (1 - \beta) w_\infty \quad (\text{S2.13})$$

$$\sum_{i \in C} E_i f_1(\tau_i x_j) + z_{1j}^+ - z_{1j}^- = y_{1j}, \quad j \in P \quad (\text{S2.14})$$

$$E_0 + \sum_{i \in C} E_i f_2(\tau_i x_j) + z_{2j}^+ - z_{2j}^- = y_{2j}, \quad j \in P \quad (\text{S2.15})$$

$$w_1 = \sum_{j \in P} (z_{1j}^+ + z_{1j}^-) + \alpha (z_{2j}^+ + z_{2j}^-) \quad (\text{S2.16})$$

$$w_\infty \geq z_{1j}^+, \quad w_\infty \geq z_{1j}^- \quad (\text{S2.17})$$

$$w_\infty \geq \alpha z_{2j}^+, \quad w_\infty \geq \alpha z_{2j}^- \quad (\text{S2.18})$$

$$z_{kj}^+, z_{kj}^- \geq 0, \quad j \in P, \quad k \in \{1, 2\} \quad (\text{S2.19})$$

$$w_1, w_\infty \geq 0 \quad (\text{S2.20})$$

$$E_i \geq 0, \quad i \in C \cup \{0\} \quad (\text{S2.21})$$

Objective function (S2.13) minimizes the approximation error. Variables  $w_1$  and  $w_\infty$  correspond to the two terms in function (S2.12). Constraints (S2.14) - (S2.15) calculate the per point approximation error: an error at each point  $x_j$  is the sum of two values ( $z_{kj}^+ + z_{kj}^-$ ); at least one of them is equal to zero. Constraints (S2.16) - (S2.18) express the norms from (S2.12) in terms of per point differences.

Note that this optimization problem is highly under-defined, i.e., formulation (S2.13) - (S2.21) has multiple alternative optimal solutions, many of them being physically insensible. There are two non-exclusive ways to overcome this.

First, considering more control points (larger set  $P$ ) narrows the set of optimal solutions. Yet, this approach is not always feasible as control points usually correspond to (scarce) experimental data.

Second, formulation (S2.13) - (S2.21) can be extended with some generic constraints. For example, one may impose a requirement that smaller values of  $\tau_i$  correspond to smaller values of  $E_i$ :

$$E_{i-1} \geq E_i, \quad i \in P. \quad (\text{S2.22})$$

Another example is imposing monotonicity of the approximating curve on some sequence of  $n$  points  $\{x_j\}_{j=1 \dots n}$  such that  $x_j < x_{j+1}$  ( $j = 1 \dots n - 1$ ). For instance,

$$\sum_{i \in C} E_i f_1(\tau_i x_j) \geq \sum_{i \in C} E_i f_1(\tau_i x_{j+1}), \quad j = 1 \dots n - 1 \quad (\text{S2.23})$$

forces function  $E''(\omega)$  to be non-increasing on interval  $[x_1, x_n]$ . In a similar way, non-decreasing or even convexity requirements can be implemented.

To sum up, for fixed  $\boldsymbol{\tau}$ , the optimal values for  $\mathbf{E}$  can be efficiently found by solving a constrained linear problem.

### A2.3.2 Optimizing $\boldsymbol{\tau}$

Thus, if optimal  $\boldsymbol{\tau}$  is known, finding optimal  $\mathbf{E}$  is rather straightforward. However, finding the former is more complicated due to the non-linearity of the corresponding optimization problem. Given that the only restriction on  $\boldsymbol{\tau}$  is non-negativity, unconstrained non-linear optimization methods can be employed at this stage with minor modifications. We use the following simple iterative algorithm that revises  $\boldsymbol{\tau}$ .

---

**Start:** Select some initial  $\boldsymbol{\tau}$ , desired precision  $\varepsilon > 0$ ,  
 set  $e^* := e := \infty$ ,  $\boldsymbol{\tau}^* := \boldsymbol{\tau}$ ,  $\mathbf{E}^* := \mathbf{0}$

**repeat** generate a random vector  $\boldsymbol{\tau}$  (see below)  
 sort  $\boldsymbol{\tau}$  non-increasingly  
 solve (extended) model (S2.13) - (S2.21)  
 $\mathbf{E}$  is a solution,  $e$  – optimal objective value  
**if**  $e < e^*$   
**then**  $e^* := e$ ,  $\boldsymbol{\tau}^* := \boldsymbol{\tau}$ ,  $\mathbf{E}^* := \mathbf{E}$

**until**  $e^* < \varepsilon$  or time limit reached

**Output:**  $\mathbf{G}^*$ ,  $\boldsymbol{\tau}^*$ ,  $e^*$  - approximation error

---

The starting values for  $\boldsymbol{\tau}$  can be chosen, e.g., by setting  $\tau_i := 1/\omega_i$ . The distribution for generating random vectors (see 1<sup>st</sup> line of the repeat-loop) must be reasonably concentrated around its mean value to intensify the search, yet have a broad domain to be able of escaping local optima. We suggest a modified normal distribution:

$$\tau_i \sim \exp(N(\ln(\tau_i^*), \sigma)). \quad (\text{S2.24})$$

The exponentiation is employed to perform a log-scale search motivated by the wide range of magnitudes of  $\tau$ -values. Note that this distribution ensures non-negativity of  $\boldsymbol{\tau}$ , and its mean gets updated as the algorithm progresses.

### A2.3.3 Implementation details

Linear programs for finding  $\mathbf{E}$  can be solved using any general-purpose LP-solver in under 1 second on an average desktop. A wide variety of solvers are available, ranging from commercial ones (CPLEX, Gurobi, etc.) to open-source solvers (GLPK, CLP, etc.). We used FICO Xpress because it was already available at the workspace, it provides a user-friendly language for expressing linear programs, it allows implementing arbitrarily complex algorithms (including the one from Section S3.2), it is faster than scripting tools (e.g., Python). Though we did not experience numerical issues, they may happen due to a wide range of values involved. In that case, an LP-solver working with exact arithmetic should be used (e.g., QSopt\_ex).

We extended formulation (S2.13) - (S2.21) with constraints imposing that  $E''(\omega)$  is non-decreasing on interval  $[10^{-2}, 1]$  and non-increasing on  $[10^2, 10^6]$  by using constraints similar to (S2.23). We also used constraints (S2.22).

The iterative algorithm is relatively robust with regard to the initial  $\boldsymbol{\tau}$ , so it can be initialized with any small non-negative numbers. Alternatively, if the number of control points coincides with the size of  $\boldsymbol{\tau}$ , the latter can be initialized as  $\tau_i := 1/\omega_i$ .

The other settings were as follows:  $\alpha = 0.1$ ,  $\beta = 0.3$ ,  $\sigma = 1$ .

#### A2.3.4 Coefficients of the Prony series

The coefficient of the generalized Maxwell model (S2.8) fitting the master curves in Figures 1c-d of the main text are given in Table S1 for PMMA and Table S2 for epoxy.

*Table S1. The values of relaxation times  $\tau_n$  and relaxation coefficients  $E_n$  of the generalized Maxwell model (S2.8) for the **PMMA** master curves in Figure 1c of the main text ( $T_r = 20^\circ\text{C}$ ).*

$n$	$\tau_n$	$E_n$
1	6.18e-01	3.56e+08
2	9.96e-02	1.50e+08
3	5.88e-02	1.50e+08
4	1.92e-02	1.50e+08
5	1.06e-02	1.50e+08
6	3.06e-03	1.50e+08
7	1.28e-03	1.41e+08
8	9.73e-04	1.39e+08
9	1.71e-04	1.39e+08
10	5.54e-05	1.11e+08
11	1.60e-05	1.07e+08
12	1.27e-05	1.07e+08
13	3.73e-06	1.07e+08
14	1.62e-06	1.07e+08
15	3.40e-07	8.59e+07

*Table S2. The values of relaxation times  $\tau_n$  and relaxation coefficients  $E_n$  of the generalized Maxwell model (S2.8) for the **epoxy** master curves in Figure 1d of the main text ( $T_r = 20^\circ\text{C}$ ).*

$n$	$\tau_n$	$E_n$
1	4.07e+00	8.66e+07
2	3.04e-01	8.65e+07
3	2.99e-02	8.65e+07
4	2.99e-03	8.65e+07
5	4.79e-04	8.65e+07
6	1.09e-04	8.65e+07
7	2.58e-05	8.65e+07

8	8.90e-06	8.64e+07
9	1.77e-06	8.64e+07
10	1.10e-06	8.64e+07

### A3 Phononic plates

#### A3.1 Geometry of the samples

Phononic plates with cruciform and spiral cavities were manufactured from pristine sheets by means of a milling machine (Benchman VMC 4000).

Two of the samples (made of PMMA and epoxy) with large cruciform cavities are referred to as Large-Cross plates. They have dimensions of 240 mm x 84 mm x 12 mm and contain 5 x 3 cavities at center-to-center distance 28 mm. The width and height of each cavity are 25.2 mm and 7 mm, respectively.

Another two samples of dimensions 112 mm x 142 mm x 2.8 mm (PMMA and epoxy) have small cruciform cavities and are referred to as Small-Cross plates. They contain four rows of cavities in the horizontal and vertical directions surrounding a square homogeneous material block (Figure 3c of the main text). The cavities of 5 mm x 1.5 mm size are arranged at 6 mm center-to-center distance. The direct mill of the milling machine caused rounded edges of radius 0.6 mm.

The final two samples (PMMA and epoxy) have spiral-shaped cuts and are referred as Spiral plates. With the dimensions of 225 mm x 125 mm x 3 mm, they contain 3 x 5 cavities in a square lattice with a pitch of 25 mm (Figure 3c of the main text). The width of each spiral-form cut is  $w = 0.6$  mm. The spirals are described in the polar coordinates as  $r(s) = R(1 - s)$ ,  $\varphi(s) = 2\pi ns$  with  $R$  denoting an external radius,  $n$  being the number of turns, and  $s \in [0,1]$  (Figure 3b of the main text). For our geometry,  $R = 12.8$  mm and  $n = 1.25$ .

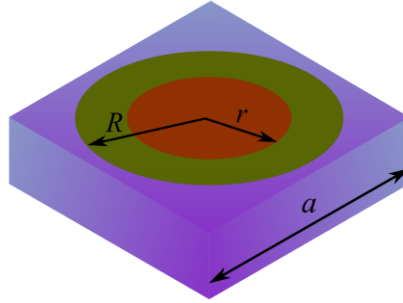


Figure A12. Unit cell of a phononic plate with polymer coated inclusions.

We also analyzed, though not manufactured, a phononic plate with coated inclusions, referred to as a Coated Inclusion (CI) plate. The unit cell of the plate shown in Figure A12 contains an epoxy-coated (green) tungsten cylinder (orange) embedded in steel (violet). The unit cell size is  $a = 15$  mm; the thickness is  $h = 2$  mm; the radii of the uncoated and coated cylinders are  $r = 5$  mm and  $R = 7$  mm. The steel and tungsten are modelled as linear elastic materials with  $K^{st} = 173$  GPa,  $G^{st} = 129$  GPa and  $K^{tg} = 311$  GPa,  $G^{tg} = 161$  GPa, respectively [17]. Epoxy is modeled as either elastic or viscoelastic. A high contrast in elastic moduli of tungsten/steel and epoxy and a one-order difference in the mass density of steel,  $\rho^{st} = 1300$  kg/m<sup>3</sup>, and tungsten,  $\rho^{tg} = 19250$  kg/m<sup>3</sup>, enable to generate a locally resonant band gap at the dipole resonant frequency of the coated cylinder [17].

## A3.2 Experimental measurements of the wave transmission

We employed two different setups to measure wave transmission in the phononic samples described in Section A3.1. Low-frequency waves in the Spiral plates are excited by means of an amplified vibration exciter (TIRA, Shaker 51110) glued to a homogeneous portion of a plate (Figure 3d of the main text). The electrical signal is transformed into out-of-plane displacements, and the frequency is swept from 300 Hz to 1.5 kHz with a sweep rate of 500 ms. The transmitted out-of-plane vibrations are recorded by a scanning laser vibrometer (Polytec, OFV 505) on the surface of the sample.

High-frequency excitation in the plates with cruciform cavities is induced by means of piezo-transducers glued to the top surface of a plate, before a phononic pattern, while the transmitted waves are acquired by a broadband piezo-sensor glued behind the pattern or by the scanning laser vibrometer. The frequency is swept in the ranges specified in Figures 4-5 of the main text with a sweep rate of 500 ms. The bounds of experimentally detected band gaps are indicated by red dashed lines and are defined here as frequency ranges at which the measured transmission drops by at least 20 dB. Note that the reference input signal amplitude is not recorded. As a result, the experimental transmittance contains an arbitrary additive constant, which shifts all transmittance values along the vertical axis. Thus, the transmission curves indicate the measured relative intensities at different frequencies and are used to highlight features in the frequency spectrum.

## A3.3 Numerical analysis

### A3.3.1 Transmission analysis

The wave transmission was calculated numerically by the Frequency Domain analysis in the Structural Module of the Comsol Multiphysics v.5.5.

The finite-element models are designed to replicate dynamic characteristics of the samples described in Section A3.1 and to reduce simulation time. Each model is represented by a plate of thickness  $h$  along the  $z$ -axis direction and of width  $a$  along the  $y$ -axis direction. To mimic the structural periodicity along the  $y$  axis, we applied continuity periodic boundary conditions at faces  $y = \pm a/2$ . In the  $x$ -axis direction, the models contain the same number of unit cells as that in the corresponding samples. Phononic patterns are surrounded by homogeneous blocks of sizes  $3a$  and  $9a$ . Structural waves are excited by harmonic displacements  $u_{z0}$  of amplitude  $1e-6$  m uniformly distributed over the top surface of a unit cell at distance  $a$  from the phononic pattern to mimic the experimental conditions. The bottom and other parts of the top faces are free of stresses. Transmitted waves are acquired at the opposite side of a phononic pattern at distance  $a$  by averaging normalized out-of-plane displacement  $20 \log_{10}(u_z/u_{z0})$ . The remaining parts of the homogeneous blocks are assigned the PML properties to reduce redundant wave reflections.

The models are fine-meshed to resolve the minimum considered wavelength by at least seven finite elements.

### A3.3.2 Dispersion analysis

The wave dispersion was analyzed under assumption of a geometric periodicity of a phononic medium. This allows restricting the consideration to a single unit cell with Bloch periodic conditions at the lateral faces [18]. For infinitesimal deformations, the equations of motion of an isotropic elastic medium are supplemented by the classic displacement-strain and constituent stress-strain relations in terms of hereditary integrals. This set of equations is then transformed into  $\mathbf{k}$ -space by means of the

Laplace-Carson transformation (see Ref. [15] for the formulas). The obtained viscoelastic boundary-value problem can be solved by applying the elastic-viscoelastic correspondence principle [14] allowing to preserve the same structure of the governing equations as that for the corresponding elastic problem provided the elastic moduli are replaced by their frequency-dependent counterparts.

For steady-state harmonic waves, the solution can be represented in terms of sets of complex-valued wave vectors  $\mathbf{k}$  at each real-valued frequency. These sets can be found by solving the following generalized eigenvalue problem:

$$(\mathbf{K}(\mathbf{k}, \omega) - \omega^2 \mathbf{M}) \mathbf{d} = 0, \quad (\text{S3.1})$$

where  $\mathbf{K}$  and  $\mathbf{M}$  are the stiffness and mass matrices, and  $\mathbf{d}$  are nodal displacements. (The derivation of this equation and representation of the matrices can be found in Ref. [15].) The Equation (3.1) was solved by means of an in-house Matlab script for fine-meshed phononic unit cells.

As an example, we analyze wave dispersion for the Large Cross epoxy plate around the Bragg band gap. In particular, we focus on waves propagating along the  $\Gamma - X$  direction as they are excited in our transmission experiments. The solutions to Equation (S3.1) can be represented as a three-dimensional plot (3D band structure diagram) with  $\text{Re}(\mathbf{k})$  and  $\text{Im}(\mathbf{k})$  along the horizontal axes, and the wave frequency along the vertical axis. Such diagrams are shown in Figure A13 for the elastic and viscoelastic (generalized Maxwell model) behavior of the epoxy. In case of the elastic material, one obtains three sets of solutions. The first set is represented by real-valued solutions,  $\text{Re}(\mathbf{k})$ , that are inversely proportional to the wavelength of a propagating wave and periodic with unique values confined within the 1<sup>st</sup> Brillouin zone (light gray curves in Figure A13a). The second set are imaginary-valued solutions,  $\text{Im}(\mathbf{k})$ , describing standing waves with exponentially varying amplitudes (light blue curves in Figure A13a). The third set is formed by complex-valued solutions that should be considered in complex-conjugate pairs and correspond to standing waves transferring no energy (blue curves in Figure A13a). The last two sets are non-periodic with values spanning from 0 to infinity. If a medium is viscoelastic, only complex-valued solutions are possible with  $\text{Im}(\mathbf{k})$  indicating the level of wave attenuation (Figure A13b).

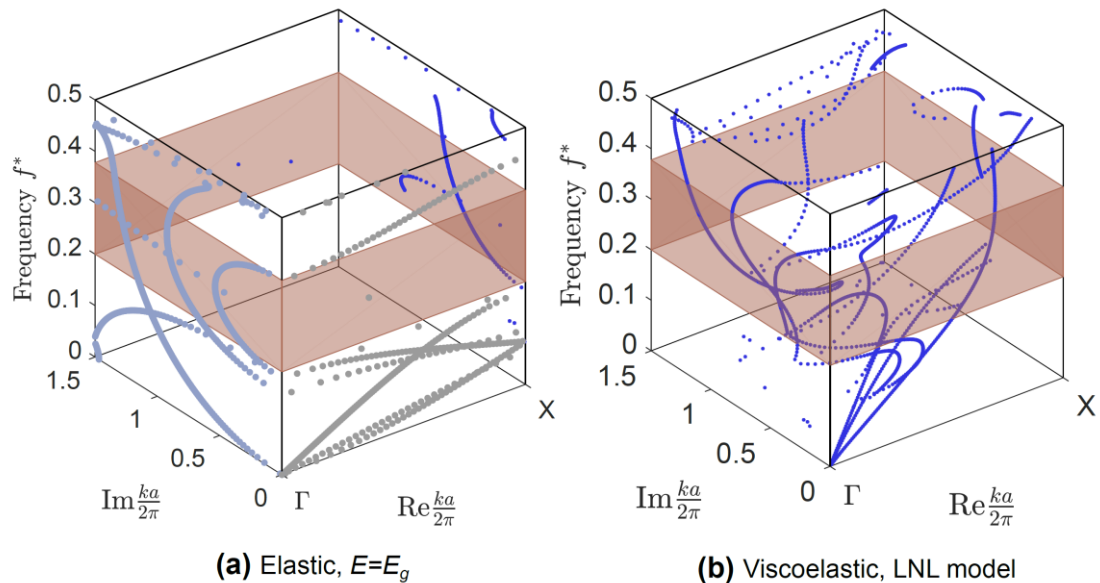


Figure A13. Wave dispersion in the **Large-Cross epoxy plate** around the Bragg band gap: Three-dimensional dispersion diagrams for propagating and evanescent waves in  $\Gamma X$  direction with (a) elastic and (b) viscoelastic behavior of epoxy. Propagating modes are shown by light gray, the evanescent modes with complex and pure imaginary wavenumbers are indicated in light-blue and blue.

Alternatively, the three-dimensional dispersion bands can be projected onto the  $\text{Im}(\mathbf{k}) = 0$  and  $\text{Re}(\mathbf{k}) = 0$  planes and thus form two-dimensional band structure diagrams (Figures A14a,b). Other examples of 2D diagrams are shown in Figures 6b,c and 7b,c of the main text. Another 3D diagram is given in Figure A15 for the Spiral epoxy plate at frequencies around the local resonance band gap.

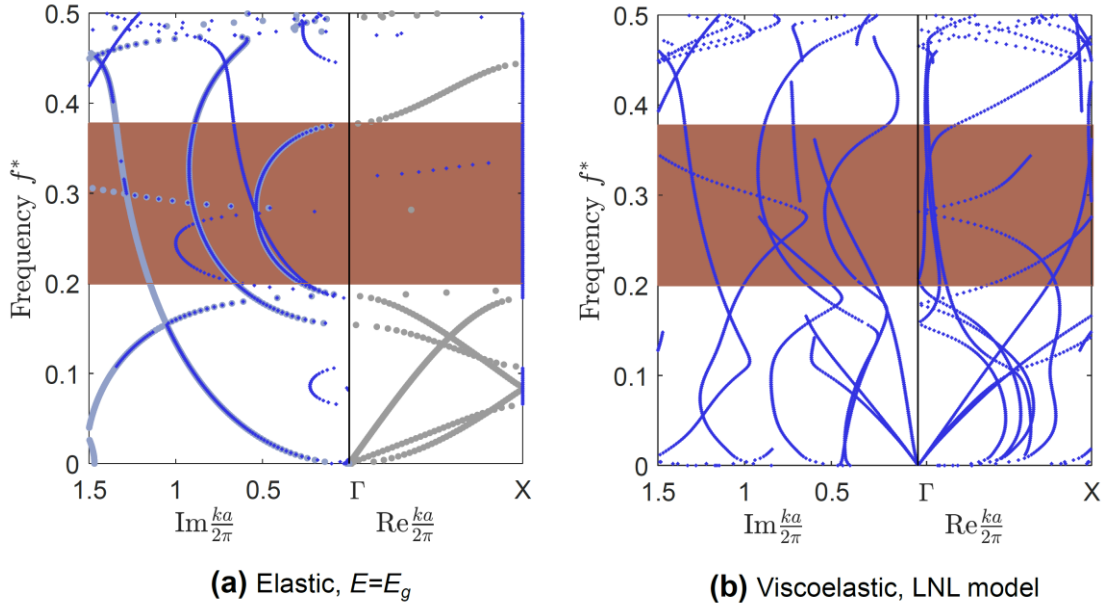


Figure A14. Wave dispersion in the **Large-Cross epoxy plate** around the Bragg band gap: Projections of the dispersion diagrams shown in Figures A13a,b for propagating and evanescent waves in the  $\Gamma X$  direction with (a) elastic and (b) viscoelastic behavior. The meaning of the colors is the same as in Figure A13.



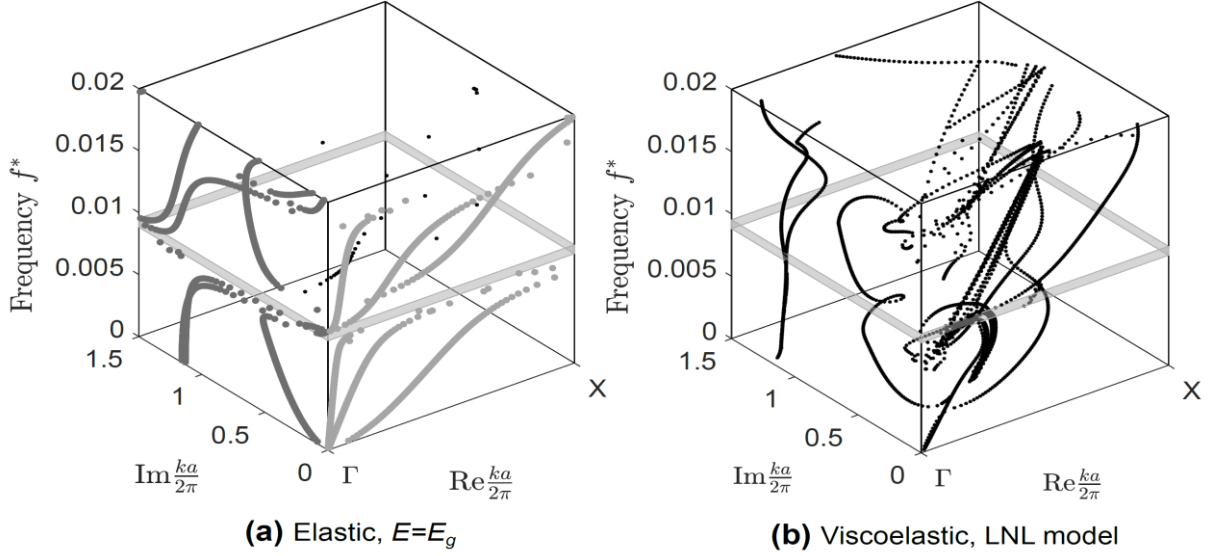


Figure A15. Wave dispersion in **Spiral epoxy plate** around a locally resonant band gap: Dispersion diagrams for propagating and evanescent waves in  $\Gamma X$  direction with (a) elastic and (b) viscoelastic behavior of epoxy. Propagating modes are shown by light gray, evanescent modes with complex and imaginary wavenumbers are indicated in gray and black, respectively. The band gap is shaded in gray.

If evanescent waves are out of interest, band structure diagrams include only propagating waves with  $\text{Im}(\mathbf{k}) = 0$ . The corresponding eigenfrequency problem can then be solved in a simpler way, by estimating frequencies  $\omega$  for each real-valued  $k$  varying along the boundaries of the irreducible Brillouin zone [17]. For a two-dimensional square lattice, this boundary is formed by the  $\Gamma - X - M$  directions in the reciprocal space [18, 19]. This approach was applied to calculate the band structure diagrams in Figures 6a and 7a of the main text for Small-Cross and Spiral plates with an elastic behavior of epoxy. The color of the bands indicates the mode polarization  $p$  evaluated as follows:

$$p = \frac{\int_V (|u_z|)^2 dV}{\int_V (|u_x|^2 + |u_y|^2 + |u_z|^2) dV}, \quad (\text{S3.2})$$

where  $V$  is the unit cell volume,  $u_x$ ,  $u_y$ ,  $u_z$  are the components of the displacement vector. The bands with dominant out-of-plane displacement  $u_z$  have the value of  $p$  close to 1 and are colored in a red palette. The modes with dominant in-plane displacements  $u_x$ ,  $u_y$  have close to zero  $p$  corresponding to a blue palette.

The frequencies in the band structures for propagating waves can be normalized as  $f^* = fa/c_p$ , where  $c_p$  is the ultrasound wave velocity in the homogeneous plate (Section A2.2). Such normalization enables to separately analyze the geometric and material wave dispersions as discussed in Section 3.2 of the main text. To illustrate the advantages of the normalization, Figure A16 shows band structures for the elastic epoxy and PMMA Small-Cross plates in non-normalized (Figures A16 a,c) and normalized (Figures A16 b,d) forms. As can be seen, the normalized diagrams, free from the information about the material properties, are visually indistinguishable confirming the identity of the architectural pattern.

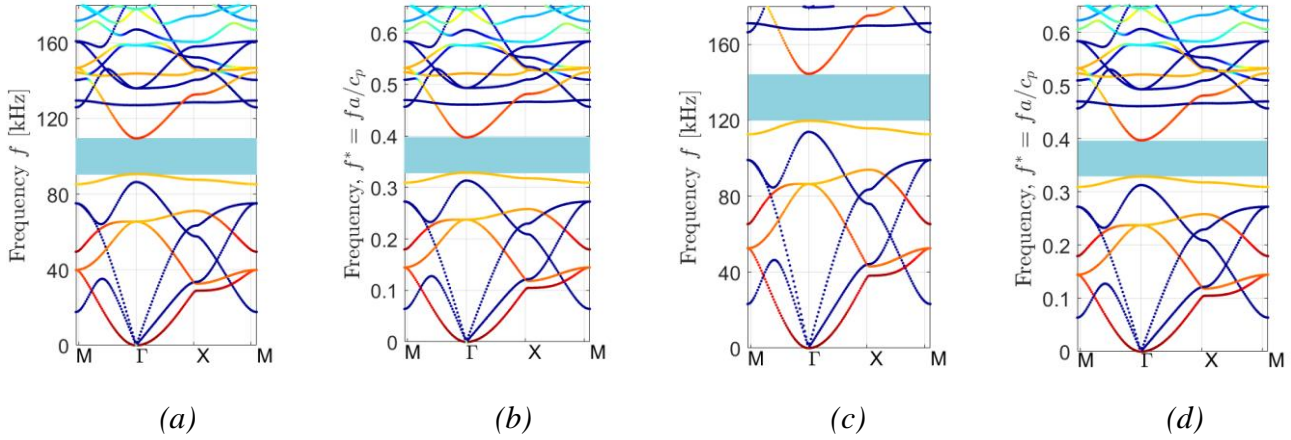


Figure A16. Band structure diagrams for **Small-Cross** plates made of **epoxy** (a,b) and **PMMA** (c,d) in terms of non-normalized  $f$  (a,c) and normalized  $f^* = fa/c_p$  frequencies.

The comparison of normalized diagrams is straightforward. For instance, Figure A17 shows two dispersion diagrams for the Small-Cross plate of different thicknesses. The plates are made of PMMA, though in the presented form, the diagrams for the epoxy plate will look the same.

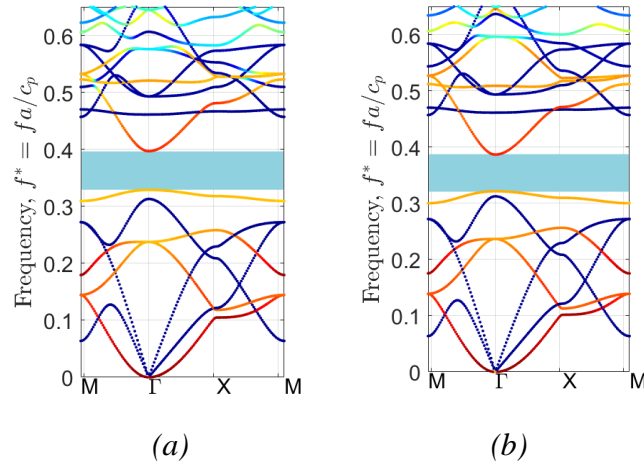


Figure A17. Band structure diagrams for elastic **Small-Cross PMMA** phononic plates of (a) 3 mm and (b) 2.8 mm thickness.

Another advantage of the normalization is to facilitate the comparison of wave dispersion in plates with identical phononic patterns and proportional structural dimensions. For instance, Figures A18 a-b show non-normalized and normalized band structure diagrams for the Large-Cross plate made of the elastic epoxy with  $E = E_g$ . The normalized diagram is identical to that of a ten-times larger plate (Figure A18d), while the dimensional band diagram for the larger plate is shown in Figure A18c. Apart from the identical band structures, the mode shapes for the bands bounding the band gaps are also identical (cf. lower sub-figures in Figure A18). This example allows us to conclude that the scaling of a phononic plate geometry, in principle, preserves its dispersion characteristics. Though, in general, this statement can be invalid, e.g., for scaling to very small dimensions when the assumption on an elastic behavior of

a medium is unapplicable.

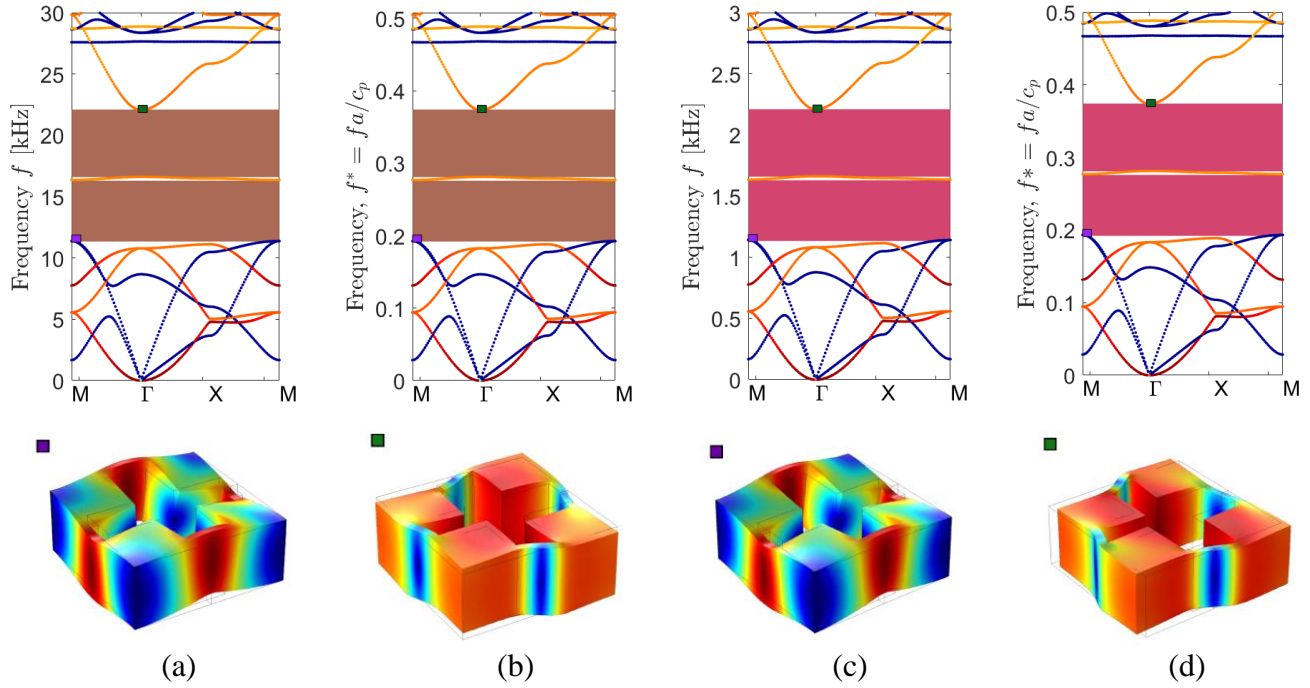


Figure A18. Band structure diagrams for **Large-Cross** (a,b) and **Large-Cross 10** (c,d) phononic plates made of **epoxy** in terms of non-normalized  $f$  (a,c) and normalized  $f^* = fa/c_p$  frequencies. The subfigures at the bottom show mode shapes at the band-gap bounds for the plates.

The dispersion bands are sensitive to the material properties of a constituent medium. This can be seen by comparing the band diagrams for the Large-Cross PMMA plate calculated for the  $E = E_g$  (Figure A19a) and the value  $E_{el}$  at the band-gap frequencies estimated directly from the master curve for  $E'$  (Figure A19b; for details see Section 3.1 of the main text). Note that the higher-order bands above the band gap are shifted to higher frequencies as the material stiffness increases. The variations below the band-gap are less pronounced as the difference in the Young's moduli is small. If this difference is larger, as, e.g., for the values of  $E_g$  and  $E_{el}$  around the locally resonant band-gap of the Spiral plate (Figures A20-A21), the variations can be observed for the whole frequency range.

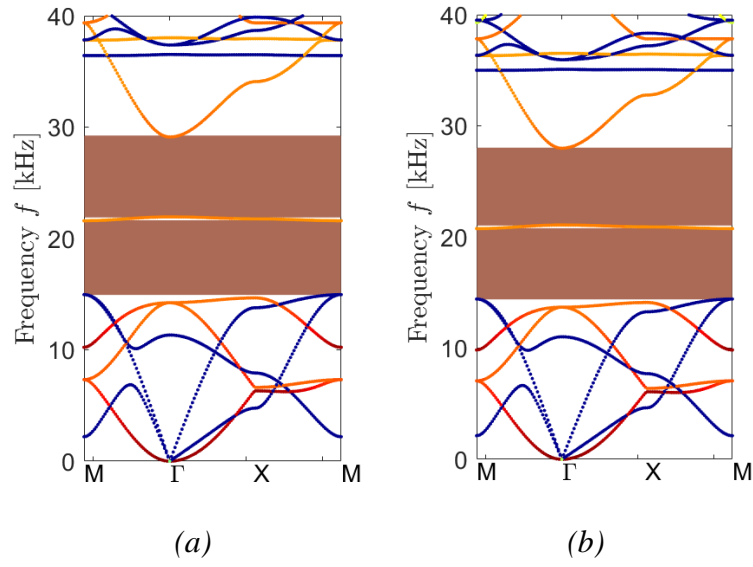


Figure A19. Band structure diagrams for **Large-Cross PMMA** plates with (a)  $E_g^{(P)}$  and (b)  $E_{el}^{(P)}$  values of the Young's modulus.

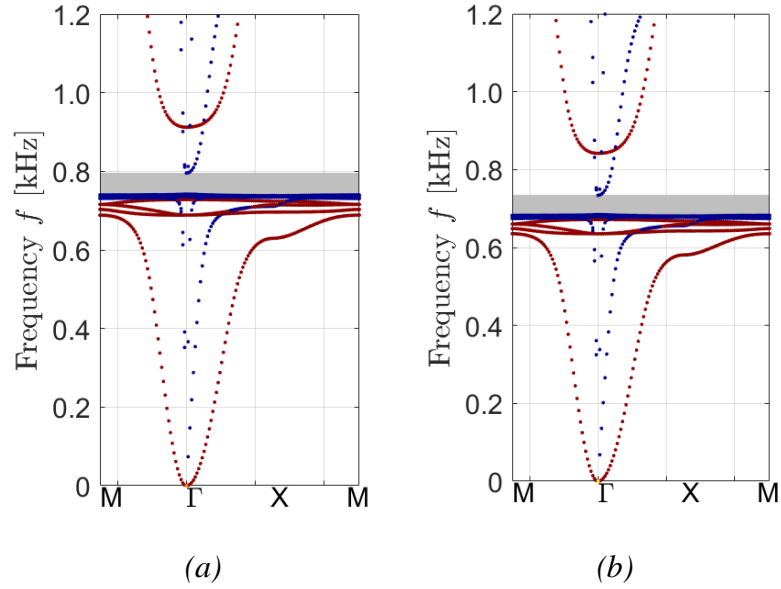


Figure A20. Band structure diagrams for **Spiral PMMA** plates with (a)  $E_g^{(P)}$  and (b)  $E_{el}^{(P)}$  values of the Young's modulus.

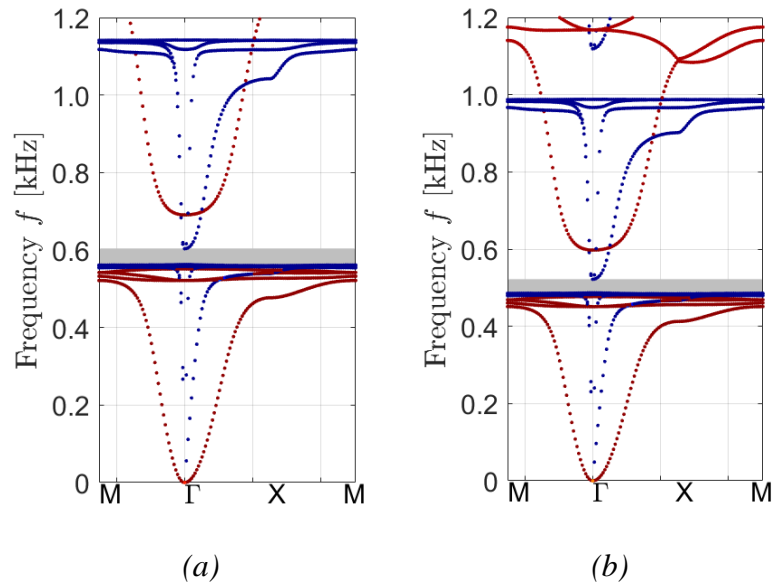


Figure A21. Band structure diagrams for *Spiral epoxy* plates with (a)  $E_g^{(P)}$  and (b)  $E_{el}^{(P)}$  values of the Young's modulus.

Finally, Figure A22 shows the band structure diagram for the phononic plate with epoxy-coated cylindrical inclusion under assumption on the elastic behavior of epoxy ( $E = E_g$ ).

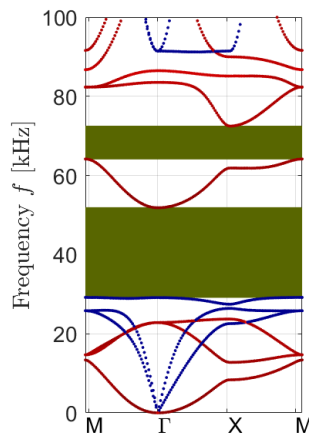


Figure A22. Band structure diagram for the phononic plate with *epoxy-coated cylindrical inclusions*. The epoxy is modelled as elastic material with  $E = E_g$ .

## Supplementary References

- [1] M. Sangermano, A. Tagliaferro, D. Foix, M. Castellino and E. Celasco, "In Situ Reduction of Graphene Oxide in an Epoxy Resin Thermally Cured with Amine," *Macromol. Mater. Eng.*, vol. 299, no. 6, pp. 757-763, 2013.

- [2] A. Grillet, J. Galy, J.-F. Gérard and J.-P. Pascault, "Mechanical and viscoelastic properties of epoxy networks cured with aromatic diamines," *Polym.*, vol. 32, no. 10, pp. 1885-1891, 1991.
- [3] C. Amaral, R. Sanchez Rodriguez, F. Gonzalez Garcia, L. Junior and E. Carvalho, "Impact of Aliphatic Amine Comonomers on DGEBA Epoxy Network Properties," *Polym. Engng. Sci.*, vol. 54, no. 9, pp. 2132-2138, 2013.
- [4] M. Aoki, A. Shundo, S. Yamamoto and K. Tanaka, "Effect of a heterogeneous network on glass transition dynamics and solvent crack behavior of epoxy resins," *Soft Matter*, vol. 16, p. 7470, 2020.
- [5] X. Shi, B. R. Hinderliter and S. G. Croll, "Environmental and time dependence of moisture transportation in an epoxy coating and its significance for accelerated weathering," *J. Coatings Technol. Res.*, vol. 7, pp. 419-430, 2010.
- [6] A. Nikolaidis and D. Achilias, "Thermal Degradation Kinetics and Viscoelastic Behavior of Poly(Methyl Methacrylate)/Organomodified Montmorillonite Nanocomposites Prepared via In Situ Bulk Radical Polymerization," *Polymers*, vol. 10, p. 491, 2018.
- [7] W. Zeng, R. Zong and B. Yao, "Kinetic Studies on the Non-isothermal Decomposition of Poly(methyl methacrylate)," *Chem. Asian J.*, vol. 23, no. 1, pp. 105-110, 2011.
- [8] C. Gracia-Fernández, S. Gómez-Barreiro, J. López-Beceiro, J. Tarrío Saavedra, S. Naya and R. Artiaga, "Comparative study of the dynamic glass transition temperature by DMA and TMDSC," *Poly, Test.*, vol. 29, pp. 1002-1006, 2010.
- [9] J. Liu, V. Garcia Sakai and J. Maranas, "Composition Dependence of Segmental Dynamics of Poly(methylmethacrylate) in Miscible Blends with Poly(ethylene oxide)," *Macromolecules*, vol. 39, pp. 2866-2874, 2006.
- [10] J. Vincent, *Structural Biomaterials*, Princeton: Princeton University Press, 2012, p. 228.
- [11] J. Ferry, *Viscoelastic Properties of Polymers*, New York: Wiley, 1980.
- [12] B. Clements, "A continuum glassy polymer model applicable to dynamic loading," *Journal of Appl. Phys.*, vol. 112, p. 083511, 2012.
- [13] B. Read, "Influence of stress state and temperature on secondary relaxations in polymeric glasses," *Polymer*, vol. 22, pp. 1580-1586, 1981.
- [14] R. Lakes, *Viscoelastic materials*, Cambridge: Cambridge University Press, 2009.
- [15] A. O. Krushynska, V. G. Kouznetsova and M. G. D. Geers, "Visco-elastic effects on wave dispersion in three-phase acoustic metamaterials," *J. Mech. Phys. Solids*, vol. 96, pp. 29-47, 2016.
- [16] A. Schrijver, *Theory of Linear and Integer Programming*, Wiley Blackwell, 1987.
- [17] A. Krushynska, V. Kouznetsova and M. Geers, "Towards optimal design of locally resonant acoustic metamaterials," *J. Mech. Phys. Solids*, vol. 71, pp. 179-196, 2014.
- [18] L. Brillouin, *Wave propagation in periodic structures*, New York: Dover, 1946.
- [19] R. Craster and S. Guenneau, *Acoustic Metamaterials: Negative Refraction, Imaging, Lensing and Cloaking*, Springer, 2013.
- [20] B. Clements, "A continuum glassy polymer model applicable to dynamic loading," *J. Appl. Phys.*, vol. 112, p. 083511, 2012.